

# JGR Solid Earth

## RESEARCH ARTICLE

10.1029/2024JB030101

### Special Collection:

Alpine mountain belts in 4-  
dimensions

### Key Points:

- The first joint tomographic model of the Alpine crust and mantle based on surface and body waves from AlpArray is presented
- A transdimensional reversible jump MCMC algorithm is implemented to directly invert for the 3D subsurface structure
- The subducting lithospheric mantle slabs are continuous, a shallow break-off is, however, within the model's uncertainty limits

### Supporting Information:

Supporting Information may be found in the online version of this article.

### Correspondence to:

E. D. Kästle,  
[emanuel.kaestle@fu-berlin.de](mailto:emanuel.kaestle@fu-berlin.de)

### Citation:

Kästle, E. D., Paffrath, M., El-Sharkawy, A., & the AlpArray and Swath-D working groups. (2025). Alpine crust and mantle structure from 3D Monte Carlo surface- and body-wave tomography. *Journal of Geophysical Research: Solid Earth*, 130, e2024JB030101. <https://doi.org/10.1029/2024JB030101>

Received 7 AUG 2024

Accepted 23 JAN 2025



### Author Contributions:

**Conceptualization:** E. D. Kästle  
**Data curation:** M. Paffrath, A. El-Sharkawy  
**Formal analysis:** E. D. Kästle  
**Funding acquisition:** E. D. Kästle  
**Investigation:** E. D. Kästle  
**Methodology:** E. D. Kästle  
**Project administration:** E. D. Kästle  
**Software:** E. D. Kästle  
**Validation:** E. D. Kästle, M. Paffrath, A. El-Sharkawy

© 2025. The Author(s).

This is an open access article under the terms of the [Creative Commons Attribution License](#), which permits use, distribution and reproduction in any medium, provided the original work is properly cited.

## Alpine Crust and Mantle Structure From 3D Monte Carlo Surface- and Body-Wave Tomography

E. D. Kästle<sup>1,2</sup> , M. Paffrath<sup>3</sup> , A. El-Sharkawy<sup>4,5</sup> , and the AlpArray and Swath-D working groups<sup>6</sup>

<sup>1</sup>Institute for Geological Sciences, Freie Universität Berlin, Berlin, Germany, <sup>2</sup>3.5 Sicherheit von Gasspeichern, Bundesanstalt für Materialforschung und -prüfung, BAM, Berlin, Germany, <sup>3</sup>Institut für Geologie, Mineralogie, Geophysik, Ruhr-Universität Bochum, Bochum, Germany, <sup>4</sup>National Research Institute of Astronomy and Geophysics (NRIAG), Helwan, Cairo, Egypt, <sup>5</sup>Institut für Geowissenschaften, Christian Albrechts Universität Kiel, Kiel, Germany, <sup>6</sup>See Appendix A

**Abstract** An ongoing controversy revolves around the detailed structure of the subducting European and Adriatic plates under the Alps and the adjacent orogens. Mostly based on P-wave travel time tomographic images, slab break-off at different times, reversals of subduction polarity and segmentation of the slab into independent units have been proposed. These processes may have important geodynamic consequences such as rapid surface uplift, past magmatic events or changes in the style of continental collision. However, some of the tomographic results are contradictory, particularly evident in the uppermost mantle where teleseismic P waves traverse the medium almost vertically with few ray crossings and a stronger dependence on the crustal correction. In this work, we present the result of an innovative joint inversion approach using surface- and teleseismic body-wave travel times to mitigate some of the shortcomings in both data types. Applying a reversible-jump Markov chain Monte Carlo approach, we simultaneously constrain the  $v_P$  and  $v_S$  structure and their uncertainties in the crust and upper mantle. The results indicate a continuous slab structure from the crust-mantle boundary down to at least 400 km depth under the western, central and eastern Alps. The results, however, also suggest that fitting the data within their respective measurement uncertainties may not be sufficient to reliably determine the presence of a shallow slab break-off beneath the Alps.

**Plain Language Summary** The ongoing convergence of European and Adriatic plates led to the subduction of the European plate under the Alps. Remnants of the subducted plate are most commonly imaged with P wave signals from remote earthquakes. The resulting tomographic images and observations at the surface have sparked a discussion on potential slab break offs, that is, removal of the deeper part of the subducting plate that may lead to surface uplift or magmatism. In this work, we present a novel approach in which we combine different data sets to resolve the ambiguities in published tomographic works and better estimate the uncertainties in the imaged structures. With the new combination of data and the applied probabilistic imaging approach, the shear and bulk velocity structure of the crust and the upper mantle down to a depth of 600 km are imaged. We find broad, high-velocity anomalies that can be traced from the crust-mantle boundary to at least 400 km depth. There is no clear indication of a break off in western, central or eastern Alps, but a conclusive answer on this questions will require further work.

## 1. Introduction

The Alpine orogenic arc is the result of the ongoing collision between the European plate with Africa and its Adriatic promontory. During convergence, most of the lithosphere of the Alpine Tethys ocean was subducted underneath Adria (e.g., Dewey et al., 1989; Stampfli & Borel, 2002). Its remnants can be imaged by seismic tomography as velocity anomalies in the upper mantle (E. Kästle et al., 2020, for a review on pre-AlpArray models). The first order structures of these tomographic models are very similar, but some aspects remain a matter of discussion, such as the connectivity of the slab anomalies with the lithospheric plates, the length of the slabs or their dip direction. These features have important implications for our understanding of the collision history. For example, slab break-offs have been proposed at different times in the geologic past to explain Alpine magmatism (~45 Ma, von Blanckenburg & Davies, 1995), uplift in the northern Alpine Molasse basin (~30 Ma in the central Alps, ~20 Ma and ~5 Ma in the eastern Alps, Kuhlemann, 2007; Schlunegger & Castelltort, 2016; Schlunegger & Kissling, 2022) or ongoing uplift in the western Alps despite the absence of convergence (<5 Ma,

**Visualization:** E. D. Kästle  
**Writing – original draft:** E. D. Kästle  
**Writing – review & editing:** M. Paffrath,  
A. El-Sharkawy

Fox et al., 2015, 2016). The idea of a slab break-off in the Eastern Alps in combination with the imaged northward dip of the fast anomaly in the mantle underneath has inspired the idea of a reversal in the subduction polarity (Handy et al., 2015; Lippitsch et al., 2003; S. M. Schmid et al., 2004, 2013; Ustaszewski et al., 2008). Even though this concept has recently become less popular (e.g., Handy et al., 2021; E. Kästle et al., 2020), it illustrates what important implications mantle tomography can have in unraveling the tectonic history.

The AlpArray experiment has brought a large momentum for the research on the Alps as a whole but seismic imaging has profited in particular from the very dense station coverage (Heit et al., 2021; Hetényi et al., 2018). In combination with methodological advances, this has led to much improved information on the subsurface structure (Paul et al., 2024). Despite the denser data coverage, discrepancies in imaged structures and their interpretations remain. Paffrath, Friederich, Schmid, et al. (2021) have found indications of recent slab detachments around most parts of the Alpine arc, while Plomerová et al. (2022) image a much shorter and connected slab anomaly in their study focused on the Eastern Alps. In addition, there is a discrepancy in location and shape between anomalies imaged from different methods, such as from surface waves (El-Sharkawy et al., 2020; E. Kästle et al., 2018) and body waves (Paffrath, Friederich, Schmid, et al., 2021; Rappisi et al., 2022). With this work, we want to address several of the issues and contribute to answering some of the open questions. By combining different data sets from Love and Rayleigh surface wave measurements and from teleseismic P and S body wave travel times it is possible to better constrain the  $v_P$  and  $v_S$  structure and thus help to get proxies on the uppermost mantle temperature and compositional variations. The structure close to the crust-mantle boundary is difficult to image with teleseismic body waves due to the very steep ray incidence. In this zone, crucial for the understanding of potential slab break-offs, surface waves can provide information and, in addition, resolve the crustal structure so that no crustal correction needs to be applied to the body wave data. In deeper parts, surface waves lack resolution due to their long wavelength whereas the shorter wavelengths of body waves have the potential to resolve smaller structures.

There are many examples of successfully joining surface and body wave data for tomographic imaging on the global (e.g., Antolik et al., 2003; Simmons et al., 2021), regional (Golos et al., 2018; Nunn et al., 2014; West et al., 2004) or local scale (e.g., Zhang et al., 2020). For the Alpine region, there are no such joint inversion models, with exception of some full-waveform tomographic models that, however, cannot exploit the full wealth of available data, due to computational constraints, and that are limited to a relatively low resolution of the Alpine slabs (Fichtner & Villaseñor, 2015; Fichtner et al., 2018; Zhu et al., 2015). The work presented herein follows a different approach within a Bayesian framework to jointly invert different data sets (e.g., Bodin & Sambridge, 2009; Zhang et al., 2020). This approach requires repeated evaluation of the forward problem, that is, obtaining travel times from a 3D  $v_P$  and  $v_S$  model, and therefore some simplifications to keep the computational effort within reasonable limits are necessary. Advantages of the method are its relative independence of user choices (however, more prior information can be provided, if desired), its ability to not just find a single model but a probability distribution of models that can explain the data and the estimation of the uncertainty of the imaged structures. In the following, we will make use of these properties and present an implementation of a direct 3D inversion approach for the Alpine subsurface.

## 2. 3D rj-McMC Tomography

The applied algorithm is based on the reversible jump Markov chain Monte Carlo (rj-McMC) tomography approach of Bodin and Sambridge (2009) and Bodin et al. (2012). An extension to the 3D case is given in Zhang et al. (2018) and to 3D joint surface and body wave tomography by Zhang et al. (2020). A purely isotropic model is assumed, but anisotropy can be included at higher computation costs as, for example, shown in E. Kästle et al. (2024). We present the basic principles of the rj-McMC method and only go into detail where it deviates from the above cited works.

We aim to obtain the probability distribution for a range of models  $\mathbf{m}$ , given an observed data set  $\mathbf{d}_{obs}$ . This so called posterior probability distribution  $p(\mathbf{m}|\mathbf{d}_{obs})$  is according to Bayes' theorem proportional to

$$p(\mathbf{m}|\mathbf{d}_{obs}) \sim p(\mathbf{d}_{obs}|\mathbf{m})p(\mathbf{m}), \quad (1)$$

where  $p(\mathbf{d}_{obs}|\mathbf{m})$  is the likelihood for the data set being obtained from a certain model and  $p(\mathbf{m})$  is the prior probability on the model parameters. The likelihood function is slightly modified from what is used in Bodin

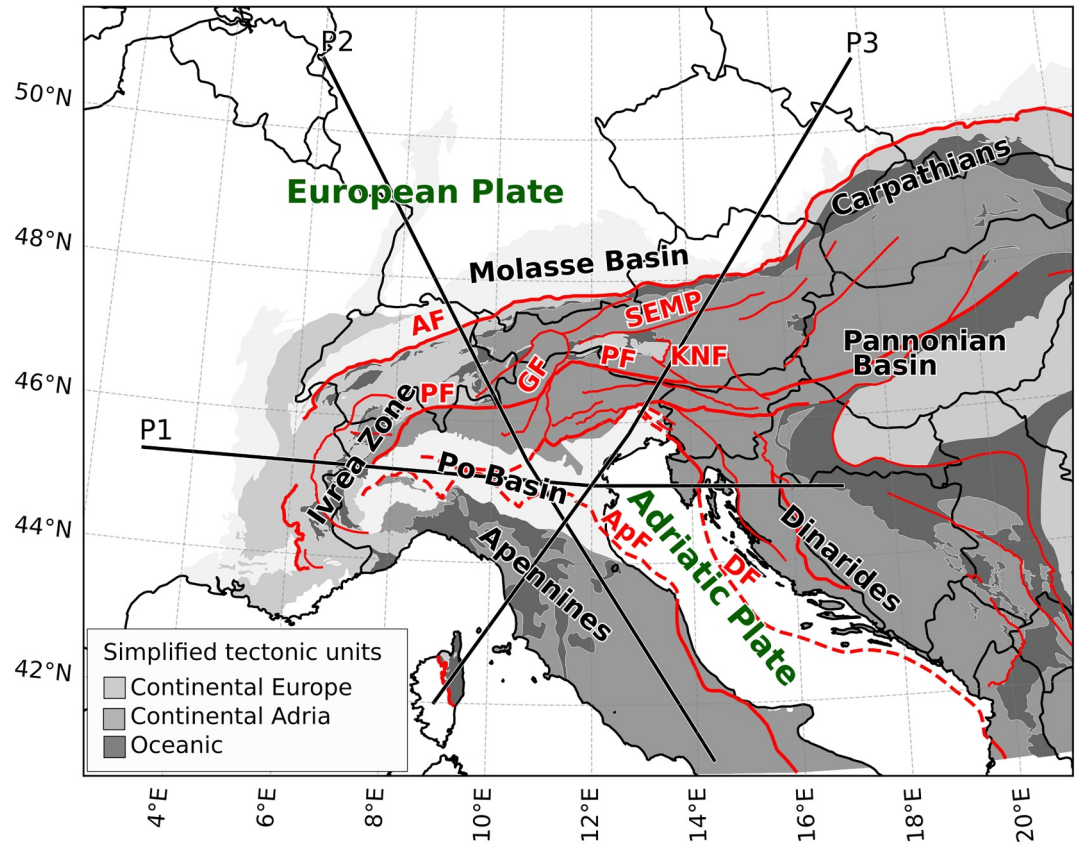


**Figure 1.** Overview of study region with major tectonic units and faults, simplified from S. M. Schmid et al. (2004, 2008) and Handy et al. (2010). The grayscale tectonic units indicate the simplified origin of the plates involved in the Alpine collision, where “oceanic” refers to remnants of different oceanic plates once separating European and Adriatic/African plates. Red lines show major faults and lineaments, where dashed means that they are not exposed at the surface. The labels P1–P3 correspond to profile traces from Paffrath, Friederich, Schmid, et al. (2021) and are discussed in this work. AF, Adriatic Front; ApF, Apenninic Front; DF, Dinaric Front; PF, Periadriatic Fault; GF, Giudicarie Fault; SEMP, Salzach-Ennstal-Mariazell-Puchberg fault; KNF Katschberg Normal Fault.

et al. (2012), by combination of a Gaussian and a uniform distribution to account for the effect of outliers (Tilmann et al., 2020):

$$p(\mathbf{d}_{obs}|\mathbf{m}) = (1-f) \frac{1}{(\sqrt{2\pi}\sigma)^N} \exp\left\{-\frac{(\mathbf{g}(\mathbf{m}) - \mathbf{d}_{obs})^T (\mathbf{g}(\mathbf{m}) - \mathbf{d}_{obs})}{2\sigma^2}\right\} + f \frac{1}{W}, \quad (2)$$

where  $f$  is the fraction of outliers (between 0 and 1) and  $W$  is the outlier width, that is, the control parameter for the uniform distribution for the values that do not originate from the Gaussian distribution. The function  $\mathbf{g}(\mathbf{m})$  describes the forward calculation of synthetic data for a given model. The total number of measurements in  $\mathbf{d}_{obs}$  is  $N$  and  $\sigma$  is the uncertainty associated with the data set. The hyperparameters  $f$  and  $\sigma$  that control the shape of the distribution are also updated during the random walks in a hierarchical way (Bodin et al., 2012; Gelman et al., 1995). In the text, we will further refer to the measurement residual which is given by

$$r = \sum_j^N |g(\mathbf{m})_j - \mathbf{d}_{obs,j}|. \quad (3)$$

Since we will work with several data sets, the total likelihood is given by the product of likelihoods from the individual data sets,  $p^{(total)}(\mathbf{d}_{obs}|\mathbf{m}) = \prod_i p(\mathbf{d}_{obs}^{(i)}|\mathbf{m})$ , so that  $N$  in Equation 2 is the number of measurements in

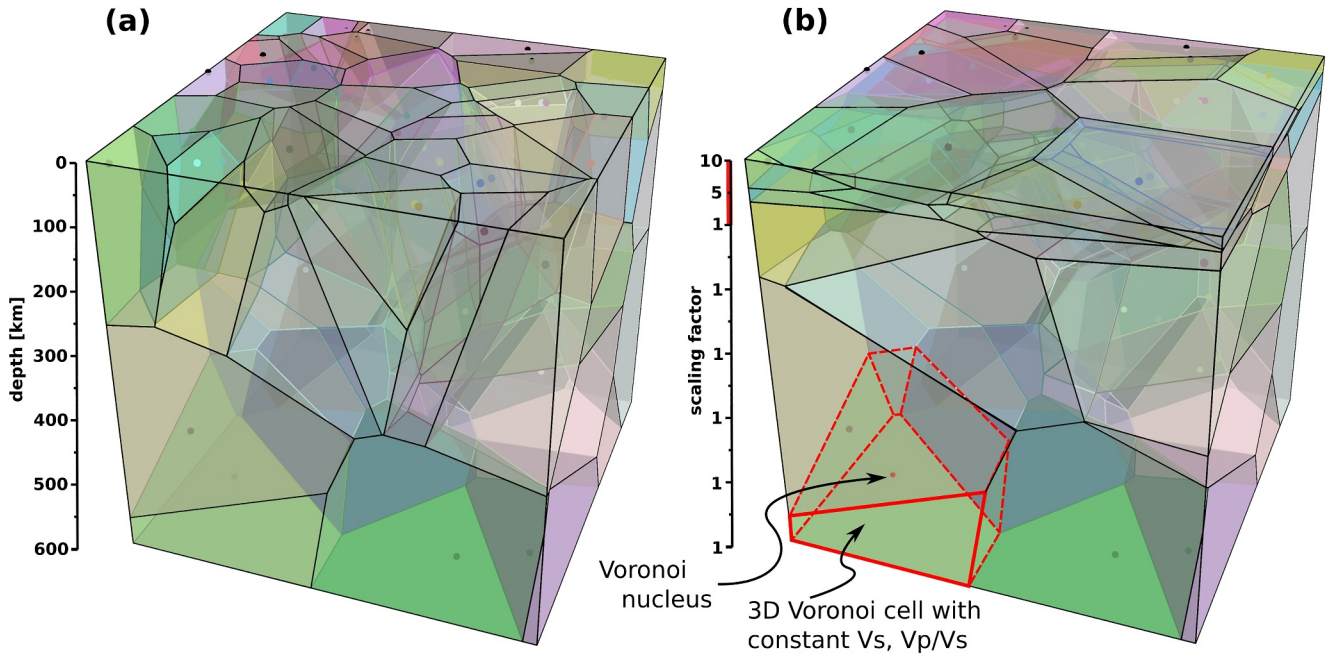


**Figure 2.** Voronoi cells in 3D. The dots inside the cells indicate the positions of the cell nuclei. (a) Standard case without vertical scaling. (b) Same positions of the nuclei, but with vertical scaling applied during the calculation of the Voronoi tessellation. The scaling factor is 10 at the surface and decreases linearly to 1 at 100 km depth.

one data set and the hyper-parameters  $\sigma_i$  and  $f_i$  can be assigned to each data set individually. The weight of a certain data point is generally controlled by the hyper-parameters  $\sigma$  and  $f$  (Equation 2). If either of these parameters is very large, there will be little influence on the likelihood from changes in the residuals. Weighting between data sets, for example, between body- and surface-wave data can thus be controlled by fixing the hyper-parameters to certain values or limiting their prior ranges. Alternatively, a similar approach as in parallel tempering can be followed where the likelihood function is exponentiated by a factor  $w$ , so that the likelihood weighted between data sets reads

$$p(\mathbf{d}_{obs}|\mathbf{m}) = (p(\mathbf{d}_{obs}|\mathbf{m}))^{w_{surf}} (p(\mathbf{d}_{obs}|\mathbf{m}))^{w_{body}}. \quad (4)$$

A factor  $w \neq 1$  has the effect as if the measurements in the data set were made  $w$  times, that is,  $w > 1$  increases the weight, while  $w < 1$  decreases the weight.

### 2.1. 3D Parameterization

The aim of this work is to image the structure in the crust and upper mantle underneath the Alps. The model is thus confined to a box that reaches from the surface (0 km) down to 600 km depth and is laterally limited by the station locations. The model space is parameterized with 3D Voronoi cells, where each cell has a constant value of the shear velocity  $v_s$  and of the  $v_p/v_s$  ratio (Figure 2). We work with an underlying, Cartesian grid of 20 km horizontal spacing and a depth spacing of 1 km at the surface that increases to a maximum of 15 km at 100 km depth and below. This reflects the decreasing vertical resolution of surface waves with depth. The Voronoi cells are defined through a nearest neighbor interpolation from the position of the nuclei onto the grid. The complete model is thus described with a model vector

$$\mathbf{m} = [(\mathbf{x}_1, \delta v_{s,1}, v_p/v_{s,1}), \dots, (\mathbf{x}_M, \delta v_{s,M}, v_p/v_{s,M})]. \quad (5)$$

For convenience, the shear velocity is given in terms relative to the prior range ( $\delta v_{s,1}$ , see below),  $\mathbf{x}_i$  contains the three Cartesian coordinates of the  $i$ -th nucleus and  $M$  is the number of Voronoi cells.

At shallow depths, typical Earth structures tend to be horizontally layered, thus Zhang et al. (2018) propose to introduce a vertical scaling factor. In this work, a vertical scaling of 10 at the surface is applied that linearly



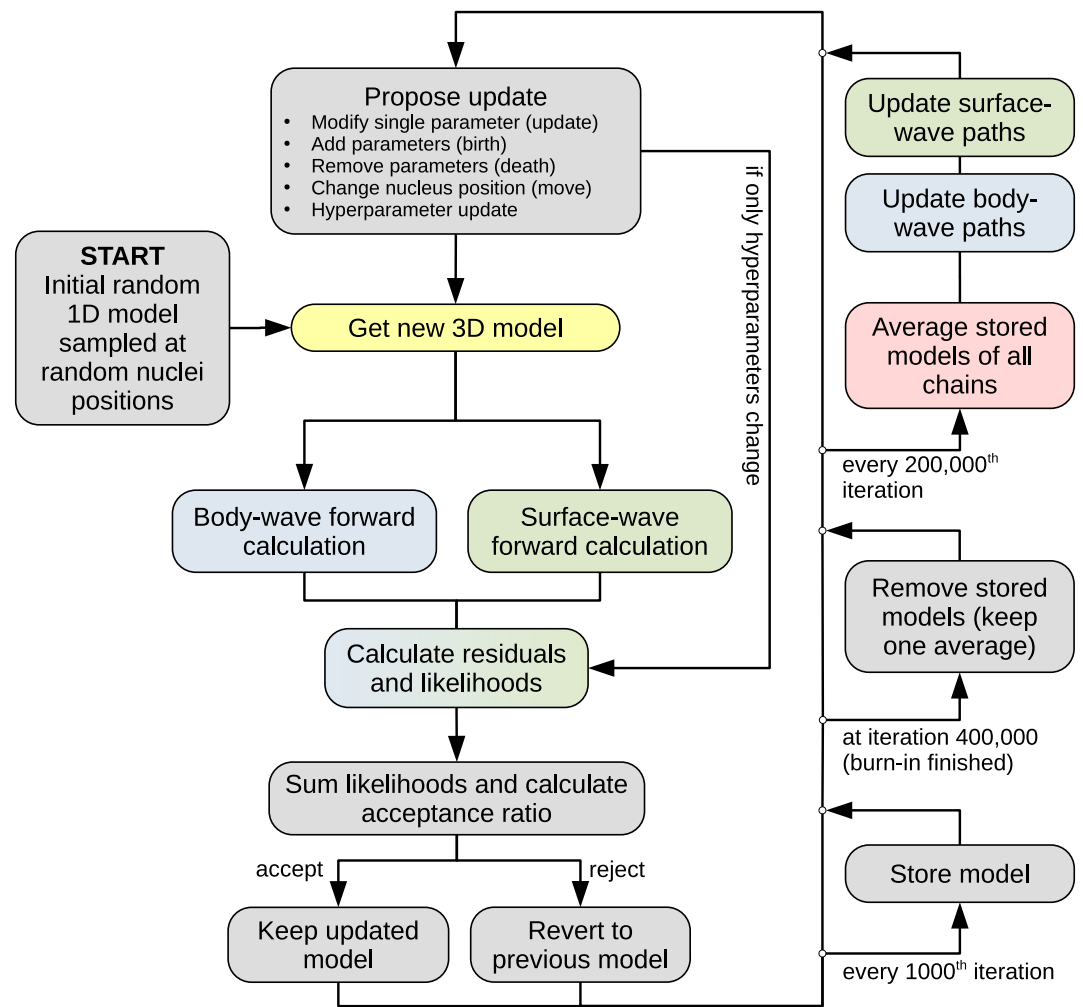


**Figure 3.** Work flow for the rj-McMC algorithm as used in this work. The search starts with an initial model and repeats the cycle for as many iterations as required. The iteration intervals on the right hand side are chosen by the user. The colors refer to different, mostly independent modules in the search algorithm. Gray describe actions performed by each chain individually. Yellow is an independent module that implements the chosen parameterization. Blue and Green represent independent modules that are responsible for performing the forward calculations and handling of the different data sets. Red is part of an overarching module that requires communication between parallel chains.

decreases to a value of 1 at 100 km depth and is constant below. An example is shown in Figure 2: The grid spacing is vertically exaggerated only during the nearest neighbor interpolation, resulting in horizontally elongated aspect ratio of the cells and improved vertical resolution. The effect of the vertical scaling is discussed in more detail in the discussion section. The algorithm described in this work is not restricted to a Voronoi parameterization, also a linear interpolation or other methods can be used. We have performed tests using a 3D wavelet transform in combination with a trans-dimensional tree structure as proposed in Hawkins and Sambridge (2015). In this case, the variable spacing of the  $z$ -axis directly controls the aspect ratio of structures without the introduction of a vertical scaling factor. It is implemented as option in the program linked in the supplement to this article, but not used in this work since it is computationally too demanding.

## 2.2. Model Search

Each individual random walk, also called a chain, starts with an initial, random model vector  $\mathbf{m}$ . For a complete posterior probability sampling, many chains will run in parallel for which the work flow is presented in Figure 3. The model vector is converted to a 3D  $v_S$  and  $v_P/v_S$  model, dependent on the chosen parameterization (Voronoi in this work). Next, synthetic travel times are calculated for body and surface waves in the current model and

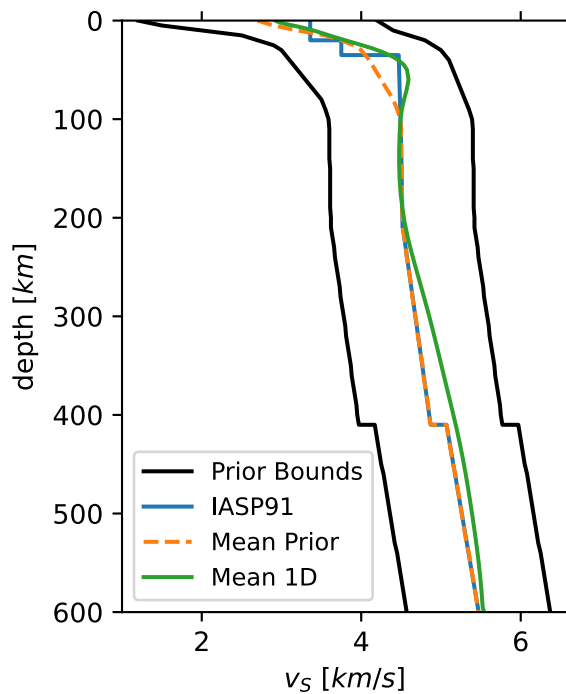


**Figure 4.** Prior on the shear velocity. The reference earth model *IASP91* is taken from Kennett and Engdahl (1991). The orange dashed line shows the mean of the prior boundaries. The green line gives the averaged 1D model at the end of the joint model search.

compared to the original measurements to obtain the residuals and the (log)likelihood (Equation 2, data sets and forward calculations are detailed in the next sections). In case of the initial iteration, the model is directly accepted, later models are accepted or rejected based on the Metropolis-Hastings acceptance criterion (Bodin & Sambridge, 2009; Metropolis et al., 1953). In the following iterations, the model is updated randomly by (a) modifying  $v_s$  or  $v_p/v_s$  in one of the cells (parameter update), (b) adding a new cell with randomly drawn  $v_s$  and  $v_p/v_s$  (birth), (c) removing an existing cell (death), (d) moving the position of one of the nuclei (move) or (e) updating one of the hyperparameters. At a birth step, the new parameters are drawn from Gaussian distributions with fixed standard deviation, centered on the mean of the parameters inside the new cell and truncated at the prior boundaries. The acceptance term when more than one parameter is drawn at the same time is given in Bodin (2010, Appendix A5).

After an initial burn-in phase, the chain starts sampling the posterior distribution. Since successive models in a Markov chain are not independent, in our case only every 1000th model is kept and used in the final ensemble of models (thinning). In regular intervals, surface and body wave ray paths are updated. For that purpose, all stored 3D models from all chains are averaged and the rays are traced in this current, average model (see details in next sections). In the model presented below, this means that the paths are only updated four times during the model search, that is, it is effectively linearized in terms of wave propagation. Galetti et al. (2015) show that updating rays at every iteration thus tracing them in each chain's current Voronoi model, yields more accurate uncertainty estimates. We expect the herein presented model to be limited in this regard. However, ray tracing and updating the corresponding matrices at every iteration for the large number of data used in this study is computationally too demanding. In addition, we expect that for long-period

surface waves this would result in unrealistically complex ray geometries if not accounting for the rays' finite sensitivity width.

Finally, after the total number of iterations is reached, the ensemble of models can be used to obtain a final, mean model, the model standard deviation or also a more detailed inspection of the posterior probability distribution.

### 2.3. Priors and Search Parameters

The 1D model used to generate the initial model is chosen randomly for each chain, but is required to have increasing velocities with depth. The initial coordinates of the Voronoi nuclei are drawn randomly according to the prior ranges: uniform in the two horizontal directions and dependent on the  $z$ -axis spacing in depth direction. The same behavior is chosen for the birth of new cells, so that due to the smaller grid spacing at shallow depths, a new cell is more likely to be placed closer to the surface. This makes sense since we expect more complex structures and have higher surface-wave resolution at shallow depths. Note that Bodin and Sambridge (2009) do not make any assumption on the distribution of gridpoints in space in their derivation, meaning that this approach does not affect the balance between birth/death steps and no modification in the calculation of the acceptance probability is needed.

The prior on  $v_s$  is chosen to have a broad range at the surface to reflect the large variability between loose sediments and solid rock. It is successively getting smaller with depth and is kept at a constant value of  $\pm 0.9$  km/s from the IASP91 reference earth model at 100 km and below (Figure 4; Kennett & Engdahl, 1991). In order to simplify the calculation of the acceptance probability during the model search, this depth dependent prior is replaced with a uniform prior on  $\delta v_s$  that varies between 0 (lower prior boundary) and 1 (upper prior boundary), independent of depth. The prior on the  $v_p/v_s$  ratio is uniform between 1.6 and 1.9 at all depths, and the number of Voronoi cells is limited between 10 and 10,000.

The prior on the data standard deviation  $\sigma$  is chosen wide enough so that the algorithm can freely converge to the optimal value (0.01–1, units in km/s or s, depending on data type, see sections below). The fraction of outliers  $f$

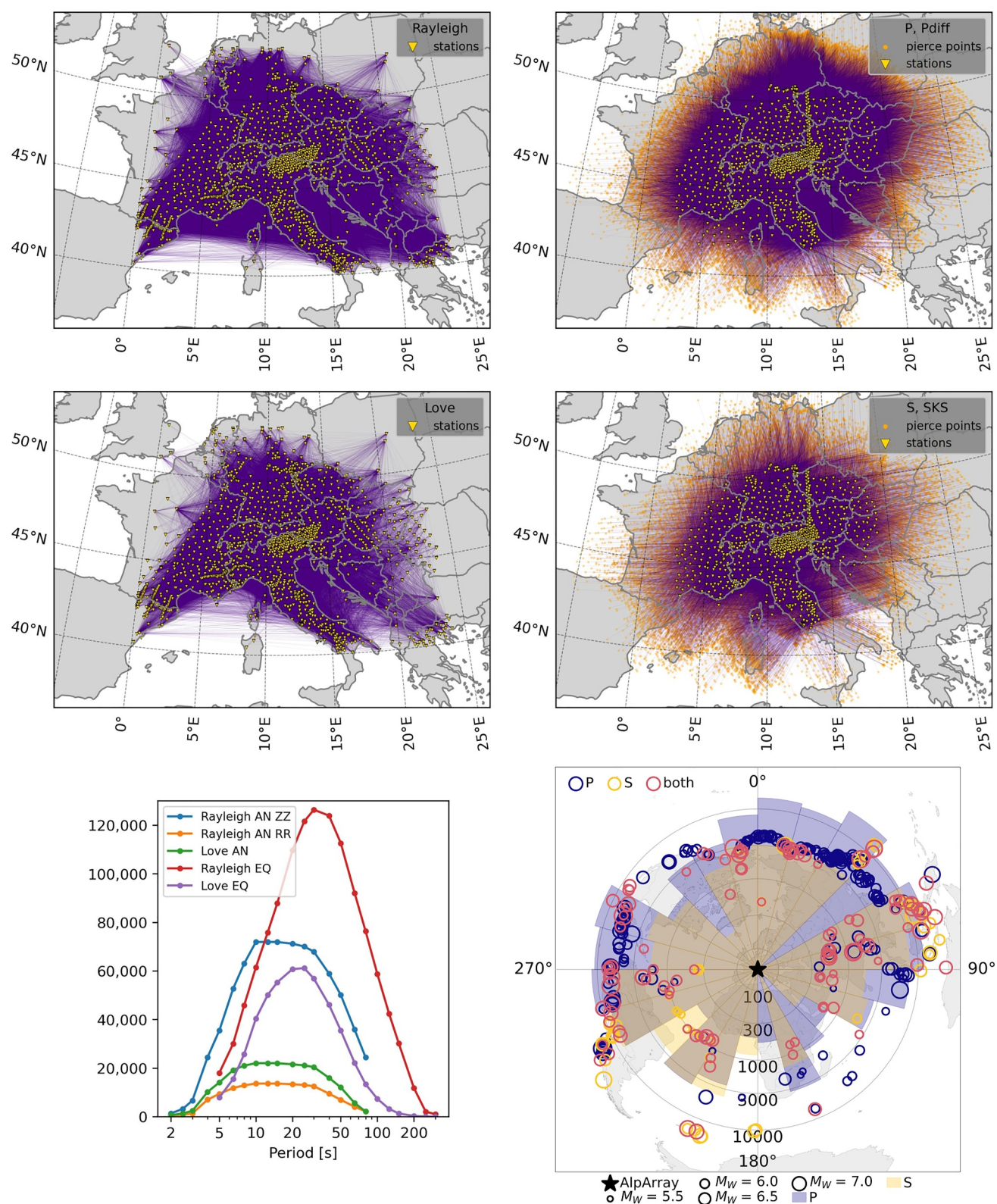


Figure 5.



can vary between 0 and 0.8. The upper boundary at 80% is set because otherwise the algorithm may get stuck at an outlier quota of 100% for very bad starting models. The width of the uniform distribution  $W$  (Equation 2) is calculated from the range of residuals resulting from a simple 1D reference model and is not changed during the model search (Tilman et al., 2020).

For parameter updates and move steps, new values are drawn from a Gaussian distribution, centered on the previous value with a standard deviation optimized so that between 40% and 50% of the proposed updates are accepted. For birth steps, the standard deviation is fixed at 0.1, both for drawing the new  $v_S$  and the new  $v_P/v_S$  parameters.

### 3. Surface-Wave Data Set

This study includes fundamental mode surface-wave measurements from ambient noise (AN) and earthquakes (EQ) signals to cover a broad period range, sensitive to structures in the topmost kilometers of the crust down to the upper mantle (Figure 5). The inter-station measurements are sampled at periods  $T = [2, 2.5, 3, 4, 5, 6.5, 8, 10, 12.5, 15, 20, 25, 30, 40, 50, 65, 80, 100, 125, 150, 200, 250, 300]$  seconds. Periods listed in italics indicates the range where data from both EQ and AN is available. The short-period end is only covered by AN data, the long period side only by EQ data. The approximately logarithmic scaling between adjacent period samples is chosen to ensure similar weights on short and long period measurements (e.g., E. Kästle et al., 2018). Both Love and Rayleigh waves are included in the analysis with the benefit of having different depth sensitivities and containing some information on the  $v_P/v_S$  ratio.

#### 3.1. Travel Time Data

The AN data set is compiled from the works of E. Kästle et al. (2018, 2022, 2024). It comprises 6 years of data collected prior to AlpArray and during the recording periods of the AlpArray and Swath-D experiments (Heit et al., 2021; Hetényi et al., 2018). Fundamental mode phase travel times are extracted from ZZ- and RR-component correlations (Rayleigh) and TT-component correlations (Love). From the pre-processed and correlated signals, the travel times are extracted based on the zero-crossing method as presented in Aki (1957), Ekström et al. (2009), and E. D. Kästle et al. (2016). The reader is referred to the original publications for more information on how the measurements are obtained. If station pairs appear in more than once of the cited works, only the most recent measurement is kept so that there is no duplicate information on any station couple. Additionally, it was required that the dispersion curves can be sampled at a minimum of 10 of the above listed periods. A broad period coverage can be taken as a proxy for the quality of the measurement. Additionally, this procedure helps to reduce the size of the total data set to limit the calculation times and the memory requirements to a reasonable range. The total number of AN travel times is 1,160,655, but it varies strongly with data set and period (Figure 5).

The EQ data set similarly provides Love and Rayleigh fundamental mode phase velocity measurements between pairs of stations from the AlpArray and the surrounding seismic networks. Recently El-Sharkawy et al. (2020) constructed a large data set of earthquake-based inter-station Rayleigh phase velocity measurements with an unprecedented lateral resolution ranging from 75 to 100 km throughout the entire Europe-Mediterranean region. In this study, we update this Rayleigh wave phase velocity measurements for the time period from 2016 to 2022 and complement them by Love wave phase velocities in a broad period range of 5–250 s. For the processing, we employed the same automated inter-station phase velocity measurement algorithm as proposed by El-Sharkawy et al. (2020) and Soomro et al. (2016), in which each station pair, approximately located on the same great-circle path, the recorded waveforms are cross-correlated and dispersion curves of fundamental modes are calculated from the phase of the cross-correlation functions weighted in the time-frequency plane according to Meier et al. (2004) and Soomro et al. (2016). The cross-correlation function is filtered with a set of frequency-dependent Gaussian band-pass filters and windowed in the time domain to minimize the effects from other signals. A rigorous quality control has been applied to the phase velocity measurements (El-Sharkawy et al., 2020). The

**Figure 5.** Overview of data sets used in this study. Distribution of inter-station surface-wave measurements given in left column. The number of measurements at each period is shown in the bottom panel. The right column gives an overview of the body-wave path geometries from the pierce points (at 600 km depth) to the stations at the surface for the P and S data sets. The map on the bottom presents the distribution of events used in this study. The polar histogram indicates the number of picks from different azimuthal directions for the P and S recordings, respectively. The radial axis indicates the number of picks in each bin on a logarithmic scale ranging from 100 to 10,000.



resulting EQ data set has a larger spatial coverage than the AN data. We only take dispersion curves that have valid measurements at a minimum of 5 of the above listed periods.

### 3.2. Ray Tracing

At the beginning of the model search, straight rays along great circle paths are used. In later stages, when updating the surface-wave paths (Figure 3), rays are traced using the Fast-Marching Method (FMM) in the respective 2D phase-velocity maps that are calculated from the 3D model. The model box is Cartesian and rectangular, therefore, station locations are transformed applying a Transverse Mercator projection to assure that the horizontal distances between receivers are approximately correct. The difference in the result between straight rays and bent (FMM) rays is overall relatively small, especially at long periods, that is, in the lower crust and mantle, where the wavelengths are large.

### 3.3. Forward Calculation

The forward calculation is performed in two steps, where in the first step, phase velocity maps are created, followed by a calculation of the phase-travel times at different periods (Zhang et al., 2018, 2020). Alternatively, linearized kernels in 2D (along a ray, e.g., Fang et al., 2015) or even in 3D could be implemented similarly within the presented methodological framework. These could be updated in regular intervals, similarly to the paths in the phase-velocity maps. Whether such an approach yields different results from the two-step method applied herein is, however, beyond the scope of this work.

The 3D  $v_S, v_P/v_S$  model is converted into a set of Love/Rayleigh phase-velocity maps by performing a 1D forward calculation for each depth profile in the model (Wathelet et al., 2020; Zhang et al., 2018). The required density information is given by an empirical relation  $\rho = 0.32v_P + 0.77$  (Berteussen, 1977). The synthetic phase travel time  $t_{syn}$  at a certain period along a chosen ray can be approximated as

$$t_{syn} = \sum_k^{K_{2D}} \frac{d_k}{c_k}, \quad (6)$$

where  $K_{2D}$  is the number of grid cells in the 2D phase-velocity map,  $d_k$  is the distance the ray travels through the  $k$ th cell and  $c_k$  is the phase velocity in that cell. Since in each interaction, only a small part of the model changes, for example, the velocity inside one Voronoi cell, a significant speed up of the forward calculation can be achieved. The phase-velocity maps are only updated at a subset of the grid indices  $k_{sub}$  for which new 1D dispersion curves are calculated. The phase travel times are updated using

$$\mathbf{t}_{syn}^{(i+1)} = \mathbf{t}_{syn}^{(i)} + \mathbf{A}_{k_{sub}} (\mathbf{c}_{k_{sub}}^{(i)} - \mathbf{c}_{k_{sub}}^{(i+1)}). \quad (7)$$

so that the times at the  $(i + 1)$ th iteration can be calculated from those of the previous iteration plus an update where only those columns/elements of  $\mathbf{A}$  and  $\mathbf{c}$  are taken into account that actually changed.

### 3.4. Likelihood Calculation

We assign each measurement type (EQ, AN), each wave type (Rayleigh, Love) and each period their own set of hyper-parameters,  $\sigma$  and  $f$  (Equation 2). This results in a total of 89 sub data sets. The likelihood function is evaluated separately for each data set and summed (in log space) to obtain the total surface-wave log-likelihood. The uncertainties on the measured travel time tend to scale with the inter-station distance which would require an additional hyper-parameter to account for this scaling (Bodin et al., 2012). To avoid this, the measured and forward-calculated phase travel times are converted to phase velocities using the currently calculated path distances from the ray tracing. The residuals and the standard deviations of the sub data sets are thus given in units of km/s.

## 4. Body Wave Data Set

Imaging the mantle with surface waves is challenging since long period (large wavelength) measurements have to be employed that have a limited resolution. Body waves from teleseismic earthquakes cross the upper mantle sub-

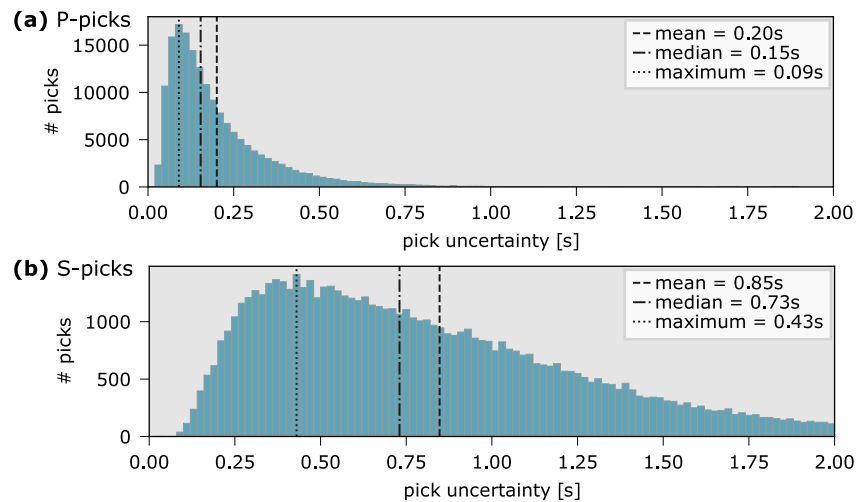


**Figure 6.** Histogram of uncertainties of the (a) P,  $P_{diff}$  and (b) the new S, SKS pick data set. Mean, median and bin with the highest number of picks are indicated by vertical lines. Details on how the pick uncertainties are obtained are given in Paffrath, Friederich, and the AlpArray and SWATH-D Working Groups (2021).

vertically and are most sensitive to structures close to the ray paths. They are therefore better suited to image for example, subducting slabs. We make use of this property by adding data sets of P,  $P_{diff}$ , S and SKS first arrival times.

#### 4.1. Travel Time Data

The body-wave data set contains a total of 170,835 first arrival travel-time picks of P and  $P_{diff}$  phases from 370 teleseismic events measured over a period of 4.5 years between 2015 and 2019, with a total of 1,025 different seismic broadband stations, most of which were part of the AlpArray Seismic Network (Hetényi et al., 2018). The multi-stage algorithm described in Paffrath, Friederich, and the AlpArray and SWATH-D Working Groups (2021) was used, which combines a modern higher-order statistics (HOS) single-station picker (Küperkoch et al., 2010) with cross-correlation. It uses the cross correlation in a first stage to align and stack waveforms around the initial HOS picks from which a high-quality (high signal-to-noise ratio) beam trace is obtained. In the second stage, the first-arrival on the beam trace is picked automatically with the HOS algorithm. The picked beam trace is used as a “blueprint” to be cross-correlated with all available station data for the event to finally correct the phase onsets. The resulting absolute arrivals have a low relative uncertainty with a median of 0.15 s. In this study, only the relative pick residuals are used. The picking procedure, the P data set and a resulting tomographic model are described in more detail in Paffrath, Friederich, and the AlpArray and SWATH-D Working Groups (2021) and Paffrath, Friederich, Schmid, et al. (2021).

A new data set of S phase onsets is derived using a slightly modified version of the same multi-stage cross-correlation picking algorithm used to generate the P-dataset. The same pool of seismic stations is used, but the event catalog (Figure 5) includes only events with epicentral distances between 35° and 75° for direct S phases and 95°–125° for SKS phases to circumvent difficulties with picking overlapping phases. The algorithm determined 69,257 picks of direct S (36,109) and SKS (33,148) phases from the horizontal components of seismic records band-pass filtered between 0.01 and 0.2 Hz. The estimated picking uncertainty of the S data set is increased by a factor of ~4 with respect to the P data set due to the lower frequency content and the S signals being obscured by the P coda (Figure 6). We choose not to use this uncertainty information in the *rj*-McMC algorithm directly, but we compare it to the data standard deviation values ( $\sigma$  in Equation 2) obtained automatically from the hierarchical approach (see Results section).

Stations located above the upper boundary of the model box (0 km) are virtually moved down by applying an elevation correction using a constant velocity ( $v_P = 5$  km/s,  $v_S = 2.8$  km/s). Stations below 0 km (ocean bottom) do not require any elevation correction since they are placed at the correct depth inside the model. To compensate for errors in the source location/timing and for velocity anomalies on the source side, a mean correction is applied

to the travel times so that only their residuals are fitted during the *rj*-McMC run. This mean correction is analog to one applied by Paffrath, Friederich, and the AlpArray and SWATH-D Working Groups (2021). From the measured, elevation-corrected travel times  $\tau$ , the mean travel time, separate for each event, is subtracted. The residual of the  $j$ -th measurement is thus

$$d_{obs,j} = \tau_j - \bar{\tau}, \quad (8)$$

where  $\bar{\tau}$  is the array mean travel time from a single event.

## 4.2. Ray Tracing

The path from the earthquake source location to the pierce point is traced in the IASP91 reference model (Kennett & Engdahl, 1991) and does not change during the runtime. The pierce point describes the location where the upcoming ray pierces the lower limit of the model box (600 km depth). As for the surface-wave case, geographic coordinates of pierce points and receiver locations are transformed to the Cartesian grid applying the same Transverse Mercator projection. Inside the model box, the initial rays correspond to those in the 1D reference model. Path updates are calculated in regular intervals (Figure 3) by tracing them in 3D with the FMM from the pierce point to the station at the surface (Figure 5). An earth-flattening transform is performed during ray tracing to account for sphericity (Müller, 1971).

## 4.3. Forward Calculation

The absolute, synthetic travel time for the  $j$ -th raypath is given by

$$\tau_j = t_j^{base} + t_j^{box} = t_j^{base} + (\mathbf{A}\mathbf{v})_j. \quad (9)$$

The travel time  $t_j^{base}$  from the source to the pierce point is pre-calculated in a 1D reference earth model (Kennett & Engdahl, 1991). The travel time inside the model box,  $t_j^{box}$ , is calculated analogously to the surface-wave case (Equations 6 and 7) and thus a similar notation is chosen where  $\mathbf{A}$  contains the distances along the raypath (size  $N_{BW} \times K_{3D}$ ) and  $\mathbf{v}$  is the vector of the absolute  $v_P$  or  $v_S$  velocities. The values inside the matrix are weighted by a sphericity-correction factor to account for the decrease in horizontal distances with increasing depth. Before inserting the synthetic times in the likelihood Equation 2 they are mean corrected (Equation 8). As for the surface-wave forward calculation, synthetic travel times can be updated much faster by applying the same logic as in Equation 7.

## 4.4. Likelihood Calculation

For the body-wave measurements, we only distinguish two sub data sets, containing P and S travel times. Accordingly, there are two sets of hyper-parameters in which the data uncertainties are given in units of seconds.

## 5. Synthetic Test

The synthetic travel time data is calculated using the 3D  $v_P$  model published in Paffrath, Friederich, Schmid, et al. (2021, Figure 7). A constant  $v_P/v_S$  ratio of 1.8 is used to generate  $v_S$ . With the same procedure as explained above, rays are traced in this model and synthetic data is obtained to which a Gaussian random error with a standard deviation of 0.25 s is added for the body-wave data and a Gaussian random error on the inter-station phase velocity of 0.08 km/s to the surface-wave data. No outliers are simulated in this data set. The *rj*-McMC algorithm is executed on 48 parallel chains for 600,000 iterations of which the first 300,000 are discarded as burn-in, and ray paths are updated every 120,000 iterations. As for the real-data case (shown below), a weight factor is introduced to compensate for the much higher number of surface-wave measurements in the data set. The weight factor  $w_{body}$  is approx. 3.8 which reflects the proportion of long-period (>30 s) surface-wave data to body-wave data (compare also Equation 4).

Two cross sections through the original and the recovered models are shown in Figure 7. To better understand the interplay of the two data sets, we conduct separate runs using only the synthetic body-wave data (Figure 7b), only the synthetic surface-wave data (Figure 7c) and a joint inversion (Figure 7d). While the first order structures are

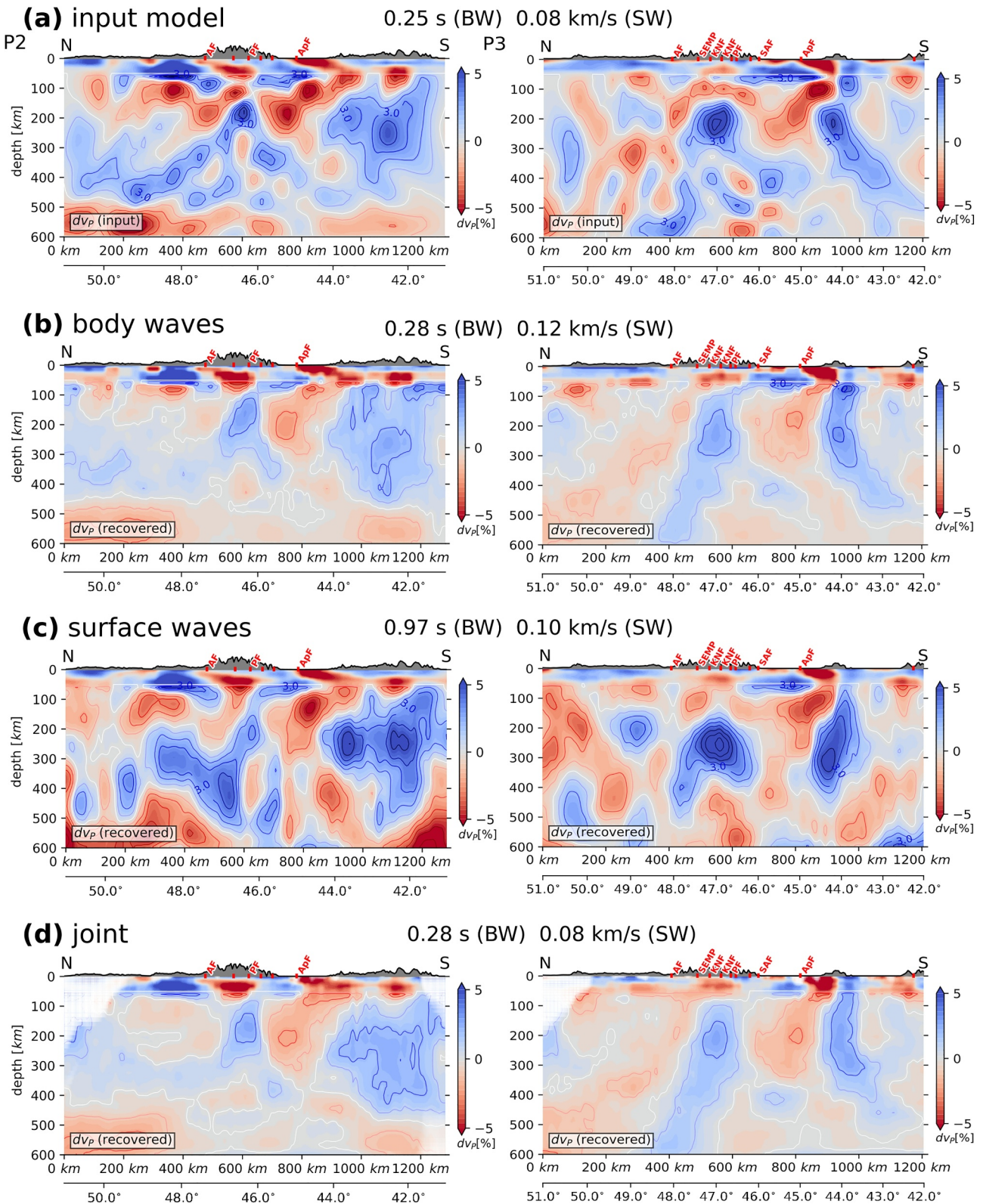


Figure 7.



similar in all resulting models, there are some important differences in some details such as the low velocity zone (slab break-off) at 100 km depth in profile P3. The body-wave model returns much smoother structures compared to the input model. Apparently, it is possible to fit the body-wave data with a data error close to the input error without fitting the small-scale and high-amplitude anomalies. In the uppermost mantle, rays are mostly running parallel in the vertical direction so that the vertical stack of low and high velocities cannot be resolved. The surface waves have a better resolution in this region and the structures look more similar to the input model in the uppermost mantle. However, below 250 km, the resolution of the surface-wave data gets low and consequently the similarity to the input model decreases significantly. Surprisingly, the joint model result resembles the body-wave-only result much more closely. This can, however, be understood when comparing the data standard deviations calculated from the final, averaged models: The numbers in Figure 7 indicate that the surface wave data have similarly good fit for models (b), (c) and (d), the body waves, however, have a clear preference for models (b) and (d). Due to the width of the surface-wave sensitivity kernels, there are more alternative models that can explain the data equally well. In the mantle, the body waves are thus more “dominant” when it comes to determining the structures. The fact that the surface-wave data fit is even a bit better for the joint model as compared to the surface-wave-only model may be related to a faster convergence in the joint model. It is simpler, therefore easier to adapt to the data and the  $v_P/v_S$  ratio is better determined by the body waves. The recovered  $v_P/v_S$  ratio in the joint model is overestimated in the crust (1.85–1.9) and underestimated in the mantle (1.7–1.75). We attribute this to a small bias in the data that is due to the different ray geometries and sensitivities. This may additionally influence the recovered structures especially in the crust-mantle transition zone.

More detailed information on the resulting model uncertainty from the synthetic tests is presented in the supplement to this article. Figure S4 in Supporting Information S1 additionally shows a synthetic test where 2%–5% outlier measurements are added to the data sets. During the inversion, the algorithm correctly estimates outlier fraction and the Gaussian data error for the surface wave data. For the body wave data, the Gaussian error is slightly overestimated and the outlier fraction tends to be underestimated.

## 6. Results

We present different results here, only inverting the P-wave travel time data set, only the surface-wave data sets and a joint inversion result. This shall illustrate the influence from the different data sets and provide the possibility to compare the results to previous works. We set up 100 (48) parallel chains that run for 1 Million (600,000) iterations of which the first 400,000 (300,000) are discarded as burn-in. The ray paths are updated every 200,000 (120,000) iterations. The values in brackets correspond to the test with just one part of the data set (only body waves/only surface waves). This is done to save computation time. According to our tests, the difference in result is relatively small as compared to the full number of iterations/chains.

### 6.1. P-Waves

Since the data set is identical to the one used by Paffrath, Friederich, Schmid, et al. (2021), we expect very similar results. For this test, the  $v_P/v_S$  ratio is fixed to values from a reference earth model (Kennett & Engdahl, 1991). Paffrath, Friederich, Schmid, et al. (2021) apply an involved scheme to constrain the crustal structure by combining different published models. During the inversion procedure, their crustal model is updated taking into account the quality of the initial model in different regions. Reproducing this setup would require some major adaptations to the workflow presented herein. Therefore, we use the final model of Paffrath, Friederich, Schmid, et al. (2021) and set it as fixed down to a depth of 65 km. The inversion will thus only fit the deeper structure.

The result is presented in Figure 8. The standard deviation of the P travel-time data set is estimated by the algorithm to be around 0.25 s ( $\sigma$  in Equation 2). This is a bit higher than the original estimate of the mean pick uncertainty (0.2, Figure 6). Note that also errors in the forward calculation (e.g., ray approximation, ray paths) or a

**Figure 7.** Synthetic test result. (a) Two sections through the input model based on Paffrath, Friederich, Schmid, et al. (2021). The section profiles are shown in Figure 1. The recovered structures averaged over all accepted models from all 48 chains are given in panels (b) and (c) for the individual data sets and in (d) for the joint data set. In the body-wave model, the crustal structure is fixed, in the other models, it is allowed to vary. A Gaussian error is added to the synthetic data of  $\text{std} = 0.25$  s for the body-wave data and  $\text{std} = 0.08$  km/s for the surface-wave data. The numbers in the center of each row give the standard deviations of the data fit for body-waves (BW) and surface-waves (SW), calculated in the averaged models. A perfectly recovered model would result in the same numbers as shown in row (a). Blue/red iso-lines give velocity perturbations.

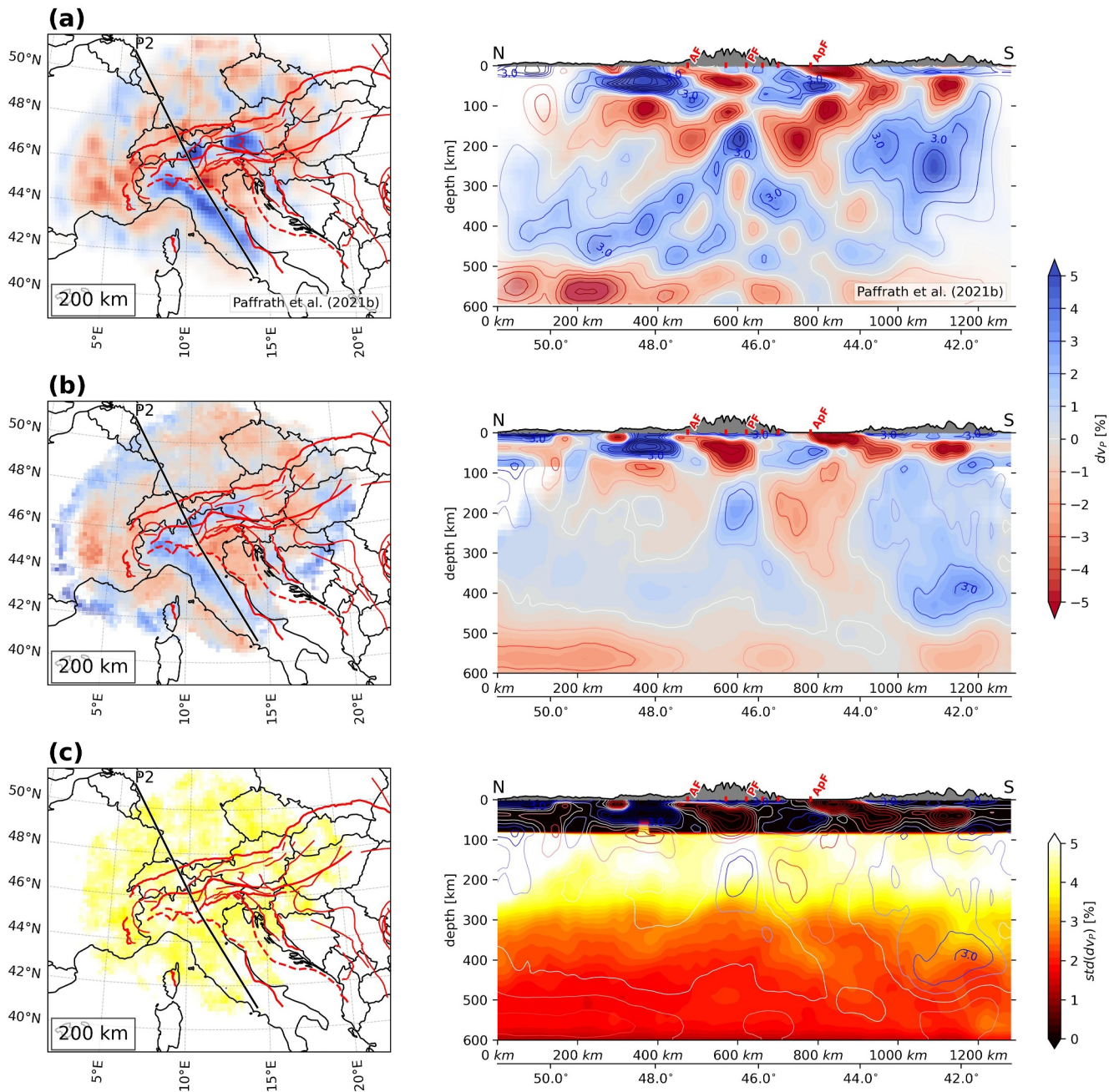


**Figure 8.** P-wave tomographic model of Paffrath, Friederich, Schmid, et al. (2021) shown in the top panels (a) compared to the one recovered from the rj-McMC algorithm (b). The model standard deviation is given in (c). The velocity variations are relative to the respective, averaged 1D velocity profile. See original publication of Paffrath, Friederich, Schmid, et al. (2021) for an explanation of regions faded to white in their model. In the bottom panels, areas with a  $v_p$  standard deviation greater 0.4 km/s are masked (model down to 65 km is fixed and has thus no uncertainty). Some smoothing is applied to the cross section plot for better comparability. Red lineaments and their labels are explained in Figure 1. The blue/red iso-contour lines indicate the velocity perturbations.

wrong elevation correction will contribute to the  $\sigma$  parameter. This may explain why it is larger than the value based on the analysis of the travel time picks. The shape of the error distribution may further be non-Gaussian as the analysis by Paffrath, Friederich, and the AlpArray and SWATH-D Working Groups (2021) and the one in Figure 6 suggest. The fraction of outliers converges to zero, thus no significant proportion of outliers is expected.

In Figure 8, only P travel time picks are used in the tomography. If the S body-wave data set is added, the P-data standard deviation ( $\sigma$ ) does not change much, meaning that a similar fit to the P data is achieved, despite the



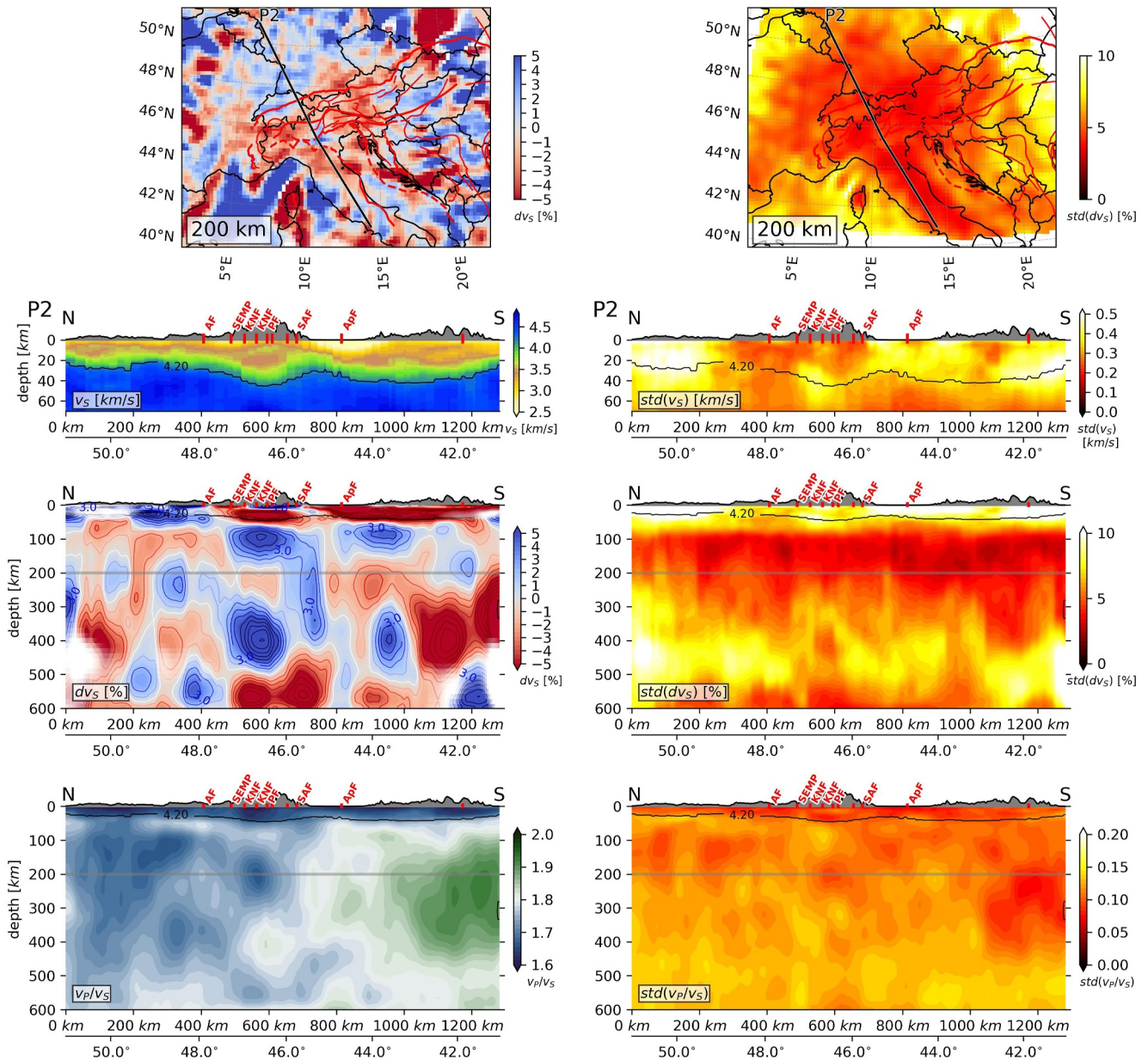


**Figure 9.** Tomographic model using only the surface-wave data sets. The left column shows different model parameters in map and profile view and the right column the corresponding parameter standard deviation. Blue/red lines in the mantle section show iso-contours of the velocity deviations. The black 4.2 km/s iso- $v_s$  line is shown in all profiles as proxy for the Moho. The thin gray line in the profiles indicates the 200 km depth level. Red lineaments and their labels are explained in Figure 1.

presence of additional S measurements. For this setup we find a value of  $\sigma \sim 0.8$  s for the S data set. The latter value is close to the mean uncertainty from the pick uncertainty (Figure 6). Images for this joint P and S model are shown in the supplement to this article (Figures S5 and S6 in Supporting Information S1).

The velocity anomaly structures in Figure 8 agree very well, the anomaly amplitudes are, however, systematically smaller in the rj-McMCM model by about 1%–2% and the structures smoother. The results are thus comparable to the synthetic results presented in the previous section and the same arguments related to the resolution of body-wave data apply. The reduced resolution of body waves in the uppermost mantle due to fewer ray crossings becomes evident when looking at the high model standard deviations above 250 km in Figure 8c. This means that the algorithm is sampling alternative structures that give a similar fit to the data, resulting in smooth, weak anomalies and a high model uncertainty. The different results of Paffrath, Friederich, Schmid, et al. (2021) and the

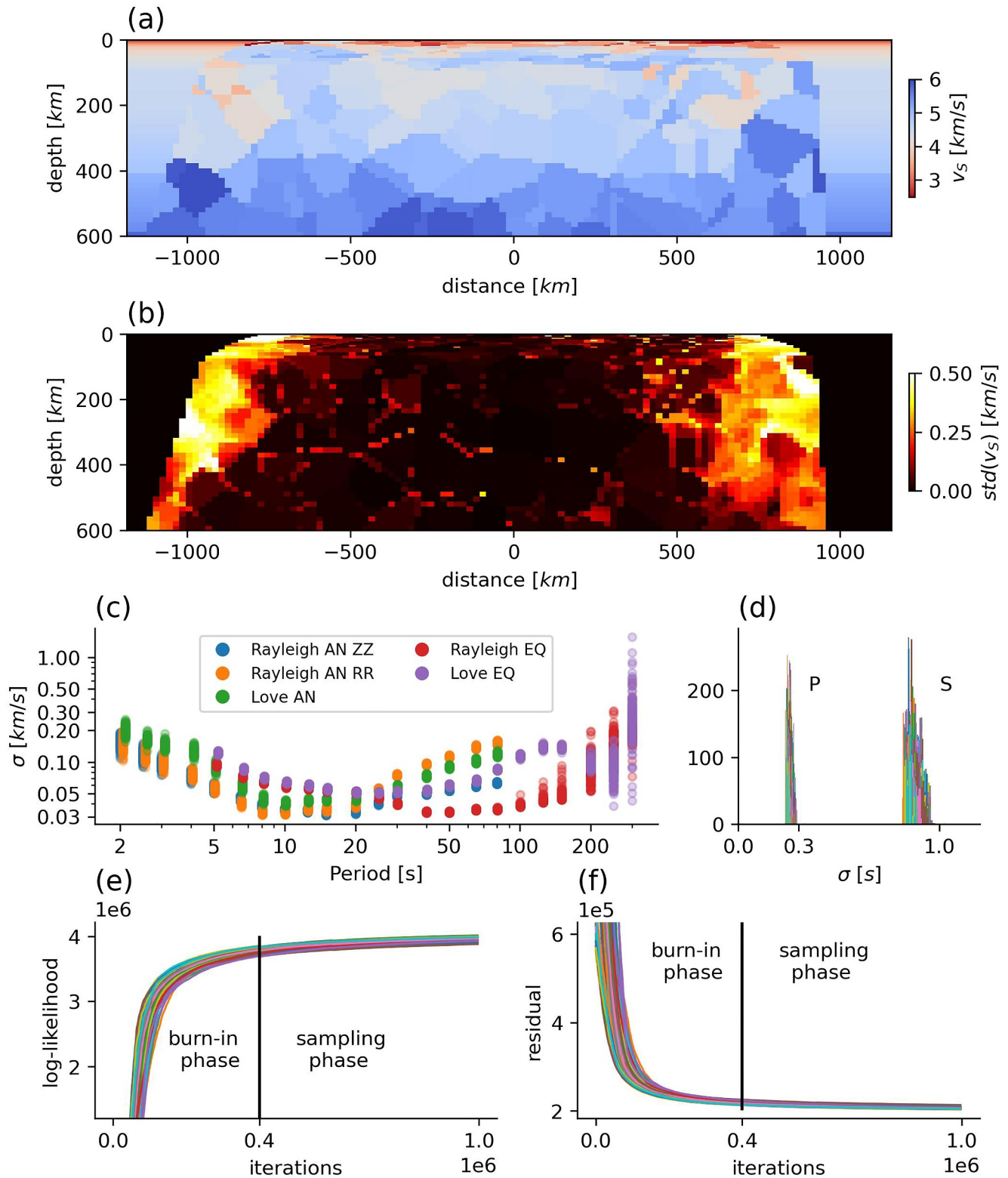


**Figure 10.** Joint inversion result. (a) Voronoi cell model from one chain during the sampling phase. (b) Model velocity uncertainty for a single chain. (c) Final data uncertainties from all 100 chains for the different surface-wave data sets. (d) Data uncertainty histograms for the two body wave data sets. Colors represent the different chains. (e) Log-likelihood evolution over 1 million iterations. Same color code as in (d). (f) Joint data residual evolution.



model in Figure 8 may thus have several reasons: In a statistical sense, the model by Paffrath, Friederich, Schmid, et al. (2021) corresponds to a maximum likelihood solution to the inverse problem, while the image from the rj-McMC model in Figure 8 is the mean of the posterior. The two would only correspond, if the posterior follows a simple Gaussian shape which is not necessary true, the distribution may be multimodal (several alternative model solutions that fit the data). Additionally, there is certainly an influence from regularization (damping, smoothing) applied to the linearized inversion and some differences in ray tracing and elevation correction. Finally, we cannot guarantee that the chains have fully converged yet, even though we find that the changes in the model become incrementally smaller when adding more iterations, suggesting that the result is already very stable. Most important for an interpretation on the subduction structure will be the relative distribution of high and low velocity anomalies. The test shows that the two models give very similar structures and thus no systematic bias from the rj-McMC approach as compared to the linearized inversion approach of Paffrath, Friederich, Schmid, et al. (2021) is expected.

## 6.2. Surface Waves

The combination of surface-wave data sets is sensitive to a very broad depth range that covers our entire model depth down to 600 km. However, at long periods, the sensitivity kernels will be broad and thus the resolution decreases with depth. The resulting model shows strong anomalies that go up to  $dv_S = 8\%$  w.r.t. the reference 1-D velocity profile (Figure 9). The model uncertainty in  $v_S$  is highest in parts of the crust because of the strong velocity variability. It is lowest in the uppermost mantle, down to about 250 km ( $\sim 0.2$  km/s) and then increases at greater depth to values of  $\sim 0.8$  km/s. Since the variability in  $v_S$  is not expected to increase significantly with depth, we assume that the increase in the uncertainties is related to the size of the sensitivity kernels that result in an only loosely constrained model at depth. From the synthetic test, we expect that the structures are not reliably resolved at depths below  $\sim 250$  km. The data uncertainties ( $\sigma$  from Equation 2) are highest at short periods ( $\sim 0.2$  km/s), lowest at intermediate periods ( $\sim 0.05$  km/s) and go up again with increasing period (up to 0.5 km/s). The trend and numbers are very similar to the full, joint inversion example (Figure 10c). We know from previous studies that AN phase travel time recordings have better quality at periods where microseisms are most energetic (7–20 s, e.g., Bensen et al., 2007). Lower measurement misfits in AN recordings between 10 and 30 s of the herein used data sets is also found by E. Kästle et al. (2018, their Fig. 3). This confirms the general trend of observed  $\sigma$  values. At short periods, attenuation and complex structures lead to an increase in data uncertainty. At long periods, the signal-to-noise ratio is generally lower for AN measurements, whereas EQ data is working with stronger signals which can explain the difference in  $\sigma$  at periods above 30 s in Figure 10.

Surface-wave data by itself only has a weak control over the  $v_P/v_S$  ratio. Nevertheless, it is a free parameter in the presented example and we find values close to the minimum prior boundary of 1.6 in the crust and a wider range of values in the mantle. There is no clear spatial correlation between low/high  $v_P/v_S$  ratio and high/low velocity anomalies in the mean model. We mainly observe a N-S splitting of low  $v_P/v_S$  ratio in the north (European plate) and higher  $v_P/v_S$  ratio in the southern part (Adriatic plate). At this point, it is unclear whether there is a physical reason behind this pattern or whether it is rather related to trade-offs between different measurements.

In the uppermost mantle, the  $v_S$  model shows higher velocities below the Alpine and the Apenninic collision zone which may represent a thickened lithosphere. The positions of the anomalies at greater depths are clearly different from those in the P-wave example (Figure 8). There are, however, some similarities to the model of El-Sharkawy et al. (2020) that also shows a fast, deep mantle anomaly directly north of the Alpine Front and between Southern Alpine Front and Apenninic Front. The data set used by El-Sharkawy et al. (2020) is similar to the EQ data used in this study.

## 6.3. Joint Data Sets

The results for a full, joint inversion show that the likelihood and the residual reach a stable plateau after approx. 200,000 iterations (Figure 10). The velocity parameters in the central areas of the 3D model do not change much in each chain after the burn-in phase, as can be seen from the single-chain model uncertainty section in Figure 10b. As in the synthetic example, a weight factor  $w_{body}$  of approx. 3.8 is applied to compensate for the larger number of long-period ( $>30$  s) surface-wave data compared to the number of body-wave data (Equation 4). The resulting model is presented in Figures 11 and 12. More images can be found in the supplement to this article, including also phase-velocity maps corresponding to the final 3D model.

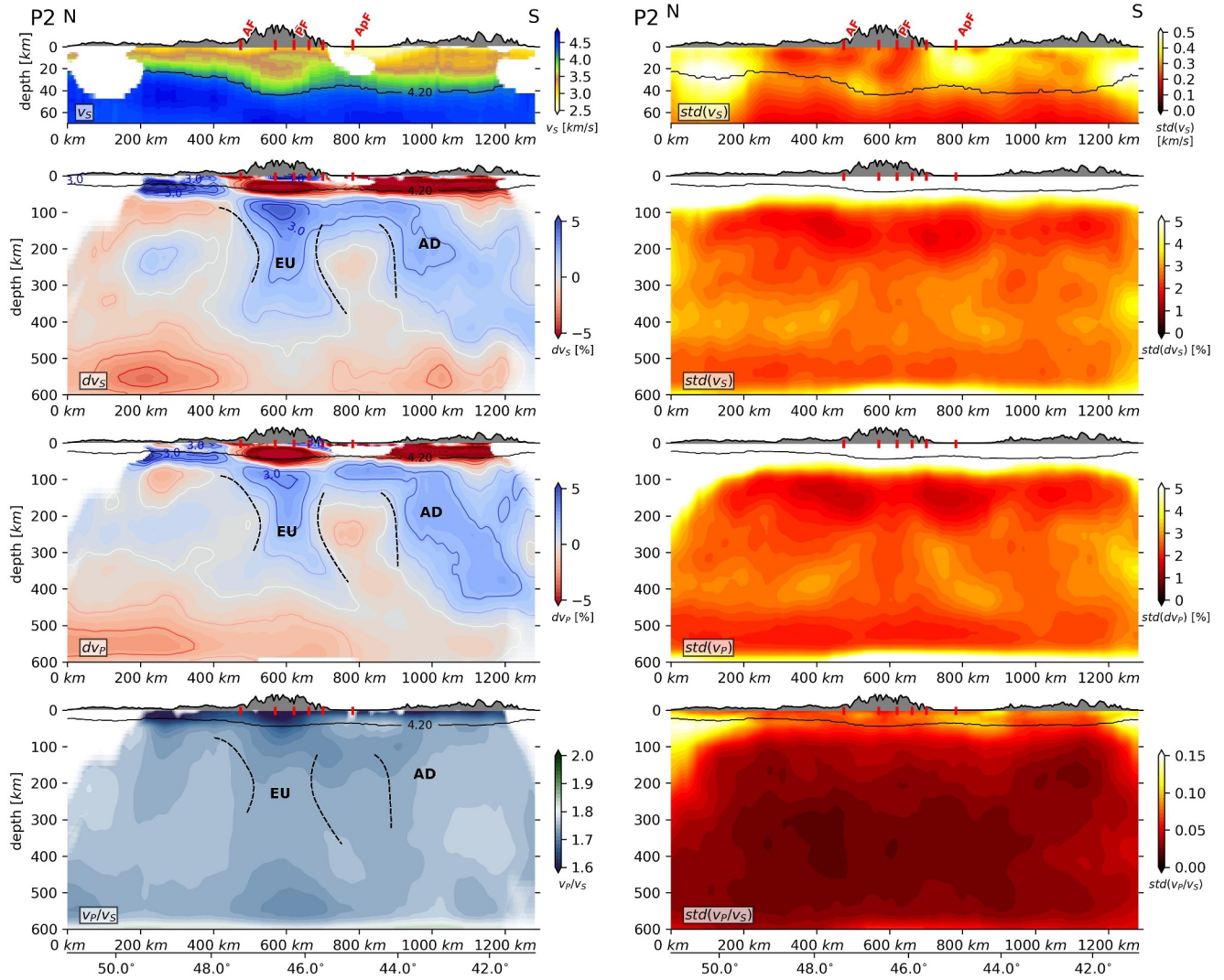


**Figure 11.** Model from joint inversion along profile P2 (see previous figures). The panels on the left side show the crustal  $v_s$  structure and  $dv_s$ ,  $dv_p$  and  $v_p/v_s$  in the mantle. Red markers at the surface correspond to the lineaments in Figure 1. Blue/red lines show iso-contours of the velocity deviations. The black 4.2 km/s iso- $v_s$  line is shown in all profiles as proxy for the Moho. Black dashed lines and labels are interpreted subducting European (EU) and Adriatic (AD) slab geometries. The labels in the  $v_p/v_s$  plot are based on the panels above and shown here for reference. Colors faded to white indicate regions of high uncertainty, that is,  $std(v_s) > 0.4$  km/s (crustal profile and  $dv_s$  profile),  $std(dv_p) > 0.7$  ( $dv_p$  profile). Additionally, in the mantle sections, regions where the ray coverage from body waves is less than 10 are hidden. The panels on the right hand side give the corresponding model uncertainty distribution along the profile.

All chains converge to very similar values for the data standard deviations for the different (sub) data sets. The surface-wave data uncertainty values are only slightly elevated, as compared to the surface-wave only example in the previous section. For the body-wave data sets, the estimated data uncertainty is 0.25 s (P) and 0.87 s (S). These values are similar to the ones obtained from an inversion where only body waves are taken into account (P: 0.25 s; S: 0.8 s, see above). The fraction of outliers estimated by the chains ranges between 2% and 4% for the surface-wave data sets and 0%/2% for the P/S picks.

On average, the surface-wave residual increases by a factor of 1.04 and the body wave residual by a factor of 1.06 when compared to the not-joint inversions. As for the synthetic example in the previous section, the body-waves seem to be more “dominant” regarding the imaged mantle structures, where we suggested that the surface-wave sensitivity kernels allow for several alternative structures in the mantle that give similarly good fit whereas the body-wave data require a more specific model, that is, have better resolution in the deeper mantle.

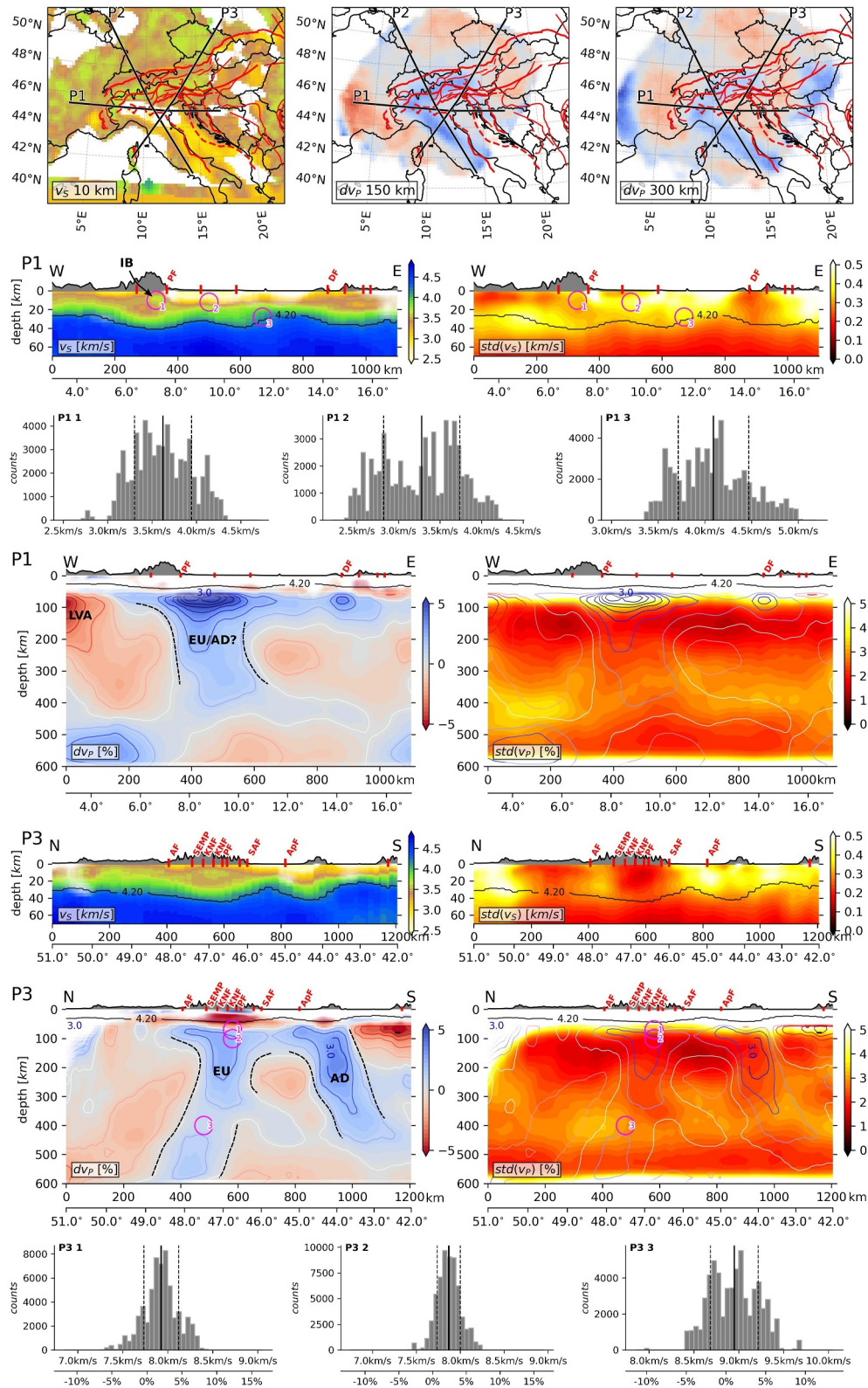


Figure 12.



In the crust, the model shows shear velocities ranging between 1.9 km/s in the sedimentary basins to 4.2 km/s which we use as a proxy for the Moho depth. The lowest velocities correspond to the Po basin region where they reach down to ~10 km depth. Low velocities are also observed in the Molasse basin, especially in southern Germany, along the Alpine Front, bordering the Czech Republic and Slovakia, in the Adriatic Sea, the Pannonian basin and southeastern France (Figure 12). The highest velocities in the shallow crust are found along the Alpine arc, close to the Periadriatic Fault zone, but also in the Bohemian massive (northern part of profile P3) and parts of the continental European crust. The crustal thickness inferred from the 4.2 km/s Moho proxy is greatest below the Alps and Apennines where it goes down to 50 km depth.

There are several fast mantle anomalies, similar in shape between  $v_p$  and  $v_s$  models that are most prominent at shallow depths, at around 100 km, and reaching to 400 km and more below the orogens. The  $v_p/v_s$  ratio is close to 1.6 (minimum prior boundary) in the crust and around 1.75 in the upper mantle. It increases again in the deepest model parts. In contrast to the surface-wave only model (Figure 9), the  $v_p/v_s$  ratio shows lower variability. Surface waves have a low sensitivity to  $v_p$  so that the  $v_p/v_s$  ratio can easily be biased, for example, by the presence of anisotropy or measurement errors. Adding body wave data therefore results in more reliable constraints on the  $v_p/v_s$  ratio. The model uncertainties are generally highest in the crust, especially at the model borders but also around velocity contrasts such as the Moho or the bottom of the sediment basins. The lowest model uncertainty is found in the depth range around 150 km depth with values lower than 0.1 km/s. The uncertainty in  $v_p$  is generally higher than the  $v_s$  uncertainty. The standard deviation of the model  $v_p/v_s$  ratio is around 0.1 in the crust and relatively stable at ~0.03 in the mantle. Higher values are only found at the model borders.

## 7. Discussion

### 7.1. Vertical Scaling Factor

The vertical scaling factor affects the shape of the Voronoi cells (Figure 2). Zhang et al. (2018) showed that the scaling factor can accelerate convergence. To better understand the effects of the chosen scaling in this work (10 at the surface, decreasing linearly to 1 at 100 km depth and constant below), we present a model without vertical scaling (Figure 13). A higher scaling gives the cells a horizontally elongated aspect ratio, therefore it is easier to image structures with strong vertical variations such as across the Moho. Consequently, the model uncertainty in the model without scaling factor is significantly increased at the Moho depth. The first order structures are, nevertheless, very similar between both models: the crust is thickened below the orogens and the sedimentary basins appear with clearly reduced velocities in the shallow crust. Differences can be found, for example, in the Ivrea region (Ivrea Body (IB) marker in Figure 12, histograms at point P1 1). From previous studies (e.g., Nouibat et al., 2022) we know that there is a shallow high velocity anomaly in the crust. This is hardly visible in the model without vertical scaling factor. The velocity histogram at this point shows a well confined distribution around mid-crustal velocities (3.5 km/s), which we assume to represent the average crustal velocity in that region. In the model including vertical scaling (Figure 12), the distribution is much broader, ranging from upper crustal velocities (3.0 km/s) to typical mantle velocities (4.3 km/s). We assume that imaging such a vertical stack of high and low velocities can be fitted much easier with horizontally elongated Voronoi cells, whereas the model without vertical scaling would need a much higher number of very densely spaced cells to capture the complex IB geometry. The difficulties in imaging the Moho interface are illustrated in the histogram in Figure 13 (P1 3): the sampled velocities result in a bi-modal distribution, with one small peak at velocities typical for the middle crust (3.4 km/s) and a larger peak at upper mantle velocities (4.5 km/s). We cannot exclude that the choice of the vertical scaling may also produce some unnecessarily complex crustal structures, but based on the comparison to previous works, we prefer the solution including the scaling factor. In principle, after long enough run times, all Markov chains should converge to the same solution, independent of the chosen scaling factor. In practice, this seems not yet to be the case after 1 Mio. iterations for such a complex and large 3D model as the examples show. In the mantle, where the scaling factor for both models is identical, the differences between the average models as well as between the velocity distribution histograms are negligible.

**Figure 12.** Final model from joint inversion. Maps and sections of the crustal structure show absolute  $v_s$  values. Mantle maps and sections give  $dv_p$  variations. Section P2 is presented in detail in Figure 11. Circles in profiles highlight regions for which the distribution of velocities are given in histograms below. The solid line in the histograms marks the mean velocity and the dashed lines the standard deviation. Red markers at the surface correspond to the lineaments in Figure 1. Blue/red lines show iso-contours of the velocity deviations. The black 4.2 km/s iso- $v_s$  line is shown in all profiles as proxy for the Moho. Black dashed lines and labels in the mantle sections are interpreted subducting European (EU) and Adriatic (AD) slab geometries. LVA, Low-velocity anomaly; IB, Ivrea Body.



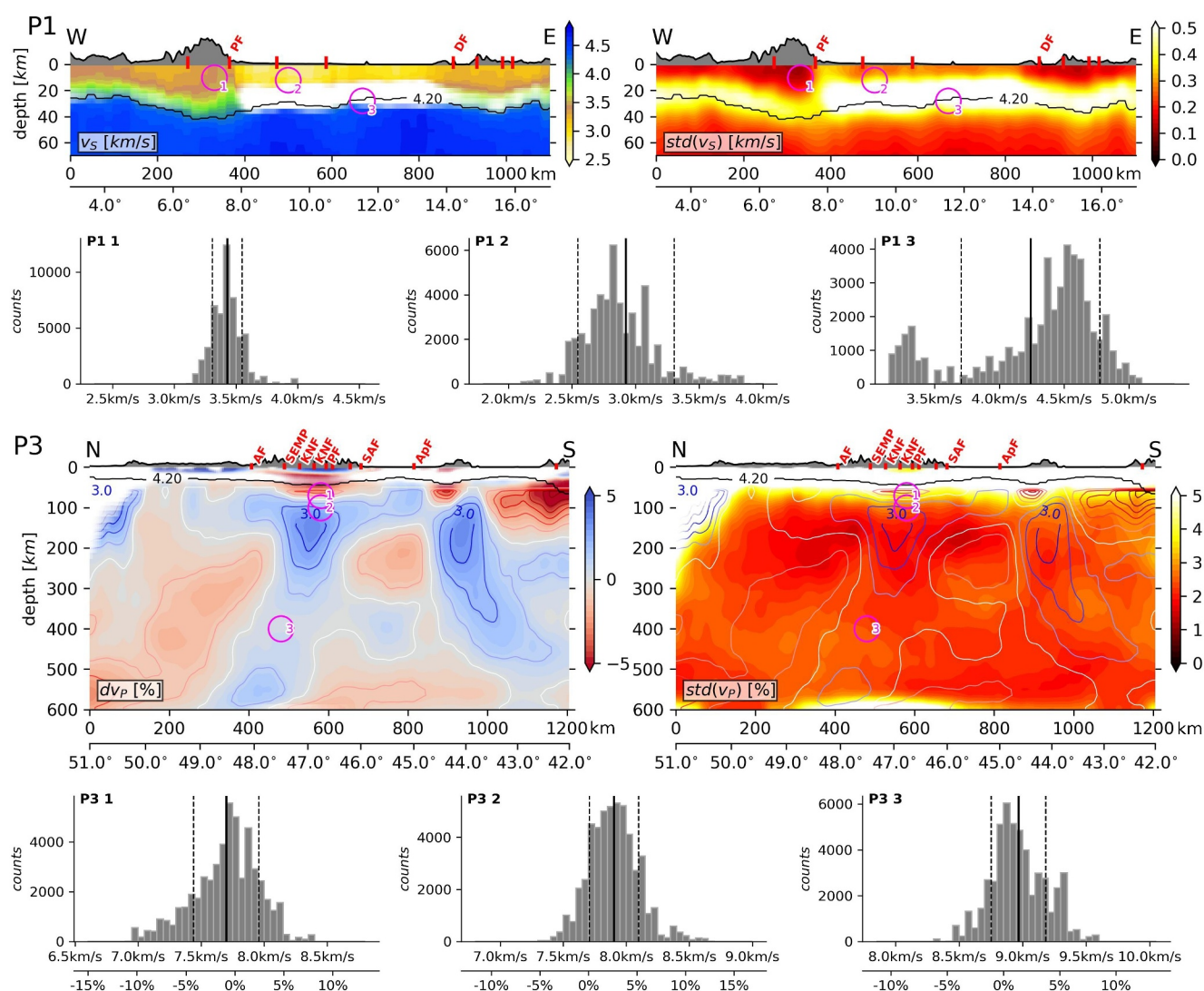


**Figure 13.** Same profiles as in Figure 12, for an inversion without vertical scaling factor. For the description of labels and markers please refer to Figure 12.

## 7.2. Assigning Uncertainties to Earthquake Events

For each body-wave data set, we assign one  $\sigma$  value that describes the uncertainty of the measured data. It would be possible to split the measurements from each event into individual sub data sets that have their own  $\sigma$  parameter for the data uncertainty. This way, the algorithm could choose to down-weight contributions from certain events that have a larger error. Our tests indicate that in this case measurements from events located in the southeast and in the northwest get assigned higher uncertainties. This corresponds to the directions where there are fewer events (Figure 5). We therefore suspect that signals coming from different azimuthal directions see slightly different velocity structures, for example, due to anisotropy. Maximizing the likelihood thus means that signals coming from azimuths with dense data coverage are preferably fitted. It is likely that events in the southeast and northwest that are assigned larger  $\sigma$  values with this approach are not actually associated with larger measurement uncertainties, but are simply down-weighted, because they do not fit well enough with the majority of the recordings from the northeast and southwest. Introducing individual event-wise uncertainties thus bears the risk of increasing the bias that comes from the non-homogenous azimuthal distribution of events. In consequence, we decided to not assign  $\sigma$  values to individual events.

### 7.3. Weighting Data Sets

Similar considerations as for the  $\sigma$  values of the two body-wave data sets can be made regarding the weighting between surface-wave recordings at different periods and with respect to the two different data types. As outlined in the previous section, the weight of a certain data set is mostly controlled by the hyper-parameters  $\sigma$  and  $f$  (Equation 2). If either of these parameters is very large, there will be little influence on the likelihood from changes in the residuals. Weighting between data sets, for example, between body- and surface-wave data can thus be controlled by fixing the hyper-parameters to certain values or limiting their prior ranges. Since finding proper values for the hyper-parameters is generally difficult, we follow a different strategy where we implement a weighting factor to compensate for the higher number of surface-wave recordings w.r.t. the body-wave data (Equation 4). In our tests, there was only little influence from the chosen weight factor on the final result so that no weighting yields very similar structures. Nevertheless, there is an influence from the selection of sub data sets so that, for example, surface-wave recordings at different periods are treated independently and have their own  $\sigma$  value. As for the body-wave case, this can lead to an artificial down-weighting of periods where only few recordings are available. However, we know also from previous studies that AN phase travel time recordings have better quality at periods where microseisms are most energetic (7–20 s, e.g., Bensen et al., 2007). Lower measurement misfits in AN recordings between 10 and 30 s of the herein used data sets is also found by E. Kästle et al. (2018, their Fig. 3). This confirms the general trend of observed  $\sigma$  values in Figure 10. We conduct additional tests (not shown) where we (a) drastically reduce the number of surface-wave data, to have an approximate equal number of measurements at all periods and (b) assign just a single  $\sigma$  value to data at all periods. For test (a), the model tends to be closer to the body-wave-only model, otherwise, we do not find significant differences in the imaged structures from these two tests.

### 7.4. Model Uncertainties

In many of the crustal sections shown in this work, the model uncertainty ranges between 0.3 and 0.5 km/s. The uncertainties are particularly high in low-velocity areas such as the sedimentary basins. This means that the structural contrasts we are interested in are often in a similar range as the modeled standard deviations. The uncertainties in the mantle are much lower, but also the structural complexity and the overall velocity contrasts are lower. In the uppermost mantle (250 km and above), the  $dv_p$  uncertainties are often between 1% and 2% whereas the imaged anomalies are around 2%–5%. Below that depth, the uncertainties and the imaged anomalies are in a similar range. This raises the questions how reliable the imaged structures are and how to interpret them.

The histograms presented in Figures 12 and 13 can give a better understanding of the mapped uncertainties. In many places, the sampled velocities do not follow a Gaussian distribution. Especially in case where we have multiple modes, the standard deviation is not a meaningful approximation to the model uncertainty. A deeper inspection of the individual Markov chains further shows that the sampled velocities are often confined to a narrow distribution, that is, the chains tend to stay in their local minima (Figure S23 in Supporting Information S1). This may lead to increased uncertainties, if chains do not converge to the same global minimum. In general, rj-MCMC methods are not efficient at sampling complex multimodal distributions (Green & Hastie, 2009). This means that a better sampling strategy could potentially lead to a more accurate reconstruction of the posterior probability distribution and thus a lower model uncertainty. For example, a smoother model parameterization, other than Voronoi cells that have sharp velocity contrasts at their borders, may facilitate transitioning between different models. In our very preliminary tests applying parallel tempering (e.g., Sambridge, 2014), or alternative parameterization schemes (e.g., Hawkins & Sambridge, 2015; Hawkins et al., 2019), we were not able to avoid this issue. The large amount of data in combination with the large number of parameters of the 3D model makes jumps between different minima in all cases very unlikely. Future studies may thus profit from a different sampling strategy (e.g., Fichtner et al., 2019; Sen & Stoffa, 2013; Zhang & Curtis, 2020, 2021). Nevertheless, we want to stress that in all our test runs, the average is very stable, if a large enough number (>40) of chains is used (an extreme case with only three chains is presented in Figure S23 in Supporting Information S1).

In the Ivrea region (histogram P1 1 in Figure 12), approximately 15% of the chains indicate mantle-derived rocks ( $v_s > 4.0$  km/s) at 10 km depth ( $v_s = 4.2$  in Nouibat et al., 2022), whereas hardly any samples are below 3 km/s. At location 2 in the same figure, at the transition between sedimentary basin and mid crust, the sampled velocities range between 2.5 km/s and 4.1 km/s; in this region, only 5% of samples are above 4 km/s. Given that for all

chains the data fit is almost identical, expressed in the value for the residual and the modeled input data standard deviation (Figure 10), we conclude that all of the sampled models that leads to the relatively broad distribution of velocity samples are equally valid. This implies that there is indeed a wide range of models that can explain the data and that a similarly high uncertainty is likely to be inherent also in other tomographic models that are based on comparable data sets (e.g., E. Kästle et al., 2018). With the 3D direct inversion approach, this uncertainty becomes more apparent, because the different 3D geometries that lead to similar travel times are sampled directly, as opposed to a separation of phase-velocity mapping and depth inversion, as it is often the case in surface-wave tomographies. Nevertheless, we can extract important information from the additional uncertainty information. For example, the model of Paffrath, Friederich, Schmid, et al. (2021) finds a low-velocity zone at 100 km depth below the Alps along profile P3, corresponding to location P3 2 in Figure 12. They interpret this as indication of a slab break-off. The models based on the joint inversion presented in this work all show velocities between  $0\% < dv_p < 5\%$ , so that the probability for a low velocity zone at this depth is relatively small. Only at shallower depth (P3 1), there is a certain number of models that also present values of  $dv_p < 0\%$ . The implications are discussed in more detail in the next section.

We therefore suggest the main reasons for the large uncertainties are (a) the difficulties in sampling a complex, multi-modal distribution, (b) the uncertainties in the measured data, and (c) the limited resolution of the data itself (broad sensitivity kernels of surface waves, sub-parallel ray geometry of body waves in the uppermost mantle) that allow for the large range of alternative models. However, there are also other factors that may play a role and that could be addressed in future studies: As mentioned above, updating ray paths only a few times during the random walks implies a major simplification, whereas Galetti et al. (2015) was able to show that taking the complex ray geometries updated at every iteration into account can yield more meaningful and more localized model uncertainties. The ray approximation may in general be too simple, especially for surface waves at longer periods. The surface-wave forward problem is solved in each iteration in two steps, that is, calculating the phase velocities in 1D depth profiles from which phase-velocity maps are created that give the phase travel times. While we estimate that this is more accurate than a completely independent calculation of phase-velocity maps and 1D depth inversion, this is not yet a direct 3D forward modeling which would ideally make use of 3D surface-wave sensitivity kernels. Also the parameterization can have an effect on the resulting model and the associated uncertainties as shown in Hawkins et al. (2019). Moreover, unaccounted anisotropy, simplifying assumptions for the heterogeneities outside the model box or the constant-velocity elevation correction may have an influence on the uncertainties.

### 7.5. Tectonic Implications

The crustal structure closely resembles that of previous ambient-noise based studies (e.g., E. Kästle et al., 2018; Lu et al., 2018). The mean velocity in the shallow crustal IB is up to  $v_s \approx 3.8$  km/s, underlain by lower velocity crustal material. This is not as high as expected from mantle material that was pushed up during the continental collision (e.g., S. Schmid & Kissling, 2000). Nouibat et al. (2022) report values of approx. 4.2 km/s and find indications of crustal subduction to a depth of 60 km. Next to the reasons already discussed in the previous section, there are several other factors that may be responsible for this difference, such as the coarser grid spacing in our model, different data types (group vs. phase velocity), less AN data in the western Alps (no CIFALPS data, Zhao, Paul, Solarino, & RESIF, 2016) and a different inversion method. Other inversed velocity structures, that is, a high velocity lens in the shallow crust underlain by lower velocities, can be observed along profiles P2 and P3, even though the contrast is much less pronounced as compared to the Ivrea zone. In the eastern Alps, such a feature has also been reported based on local-earthquake tomography under the Tauern window (Jozi Najafabadi et al., 2022). They attribute the high velocities at shallow depth to European basement nappes exhumed and exposed at the surface (Jozi Najafabadi et al., 2022, and references therein). Alternatively, there may be Adriatic lower crustal material pushed up during collision and Adriatic indentation that is sandwiched between European crustal material, thus resulting in the anomalous velocity profile. Such a model was first proposed by Lüschen et al. (2004, “Crocodile model”) for the structure underneath the eastern Alpine TRANSALP section where the material was supposedly pushed up along the “Tauern ramp.”

In the uppermost mantle, the joint model shows a layer of higher velocities below the Alps, Apennines and Dinarides which may be related to a thickened lithosphere to a depth of approx. 150 km. In the western part of the model (P1 in Figure 12, Massif Central) there is a clear low-velocity anomaly (LVA) in the uppermost mantle, similarly found by Zhao, Paul, Malusà, et al. (2016) or Rappisi et al. (2022). This may represent asthenospheric



upwelling. We interpret the fast anomalies below the orogens, reaching deeper into the mantle as resulting from subducting European and Adriatic lithospheric plates. The  $v_P$  anomalies lead almost vertically down to a depth of  $\sim 400$  km and even deeper along profile P3. The imaged  $v_S$  anomalies seem to be more pronounced at greater depths when compared to  $dv_P$ , visible also in the low  $v_P/v_S$  ratio. We assume that a potential discrepancy between surface- and body-wave data lead to the reduced  $v_P/v_S$  ratio in the deep part of the model. The surface-wave model prefers strong  $dv_S$  anomalies (Figure 9) while the P-wave model has a better fit for moderate  $dv_P$  anomaly strengths (Figure 8). The best, joint data fit is thus often obtained with a low  $v_P/v_S$  ratio. In general, there is no clear relation between the subduction structures (slabs, return flow) and the  $v_P/v_S$  ratio. When only inverting body-wave data, the European slab shows a slightly lower  $v_P/v_S$  ratio as compared to the surrounding mantle, however, this is not true for the Adriatic slab (Figure S6 in Supporting Information S1). In the surface-wave-only model, the opposite is the case, where the subducting slabs give rather high  $v_P/v_S$  values. The first order trend seems to be a high  $v_P/v_S$  ratio below the Adriatic plate and a low  $v_P/v_S$  ratio below the European plate. Surface waves are, however, not very sensitive to  $v_P$  so that we don't expect the values to be well constrained. There is little information from previous studies on the  $v_P/v_S$  structure under the Alps (e.g., Giacomuzzi et al., 2012; Koulakov et al., 2009), but these do indeed find some correlation between the slab positions and a low  $v_P/v_S$  ratio. We therefore suspect that the final, joint  $v_P/v_S$  model is dominated by trade-offs between surface and body-wave data. More accurate structures may thus be obtained by better constraining the  $v_P/v_S$  ratio in the mantle. Nevertheless, our preliminary tests with fixed  $v_P/v_S$  ratios (not shown) indicate that the overall geometries of the velocity anomalies are barely influenced by the chosen  $v_P/v_S$  ratio.

The imaged slab anomalies from the joint model are broader and smoother as compared to results only based on P-wave travel times (e.g., Mitterbauer et al., 2011; Paffrath, Friederich, Schmid, et al., 2021; Zhao, Paul, Malusà, et al., 2016). This is partially related to the addition of surface waves and the width of the long-period ray sensitivities, but also the body-wave data set itself yields smooth structures (Figure 8 and Figure S5 in Supporting Information S1). The imaged slab shapes in the joint model are thus more similar to the ones obtained from full-waveform tomography (Fichtner et al., 2018; Thrastarson et al., 2024; Zhu et al., 2015), which similarly include information from surface and body waves. This may also be related to the different tomographic imaging methodology where each chain independently cycles through alternative models, leading to smoother structures in the averaged model.

The existence of slab gaps under the Alps, indicating slab break-offs at different times in the past, is highly debated (e.g., Lippitsch et al., 2003; Mroczek et al., 2023; Paffrath, Friederich, Schmid, et al., 2021; Plomerová et al., 2022; S. M. Schmid et al., 2004). While the original idea came up to explain Alpine magmatism (von Blanckenburg & Davies, 1995), the more recent discussion has mostly evolved around tomographic images from first arrival P-wave travel times. The tomography of Paffrath, Friederich, Schmid, et al. (2021, Figure 8) suggests a shallow detachment of the European slab at a depth of  $\sim 100$  km while others show a rather continuous slab anomaly (e.g., Plomerová et al., 2022; Zhao, Paul, Malusà, et al., 2016). The dependence of P travel-time tomographies on the chosen crustal correction and the limited resolution in the uppermost mantle due to the sub-vertical incidence makes it difficult to resolve this controversy without adding more information. With the addition of surface-wave data we expect more reliable images in the crucial crust-mantle transition zone. In the joint model there are no structures giving a clear indication of a slab break-off. The histogram in Figure 12 at location P3 2 shows almost no samples at negative  $dv_P$  values. Nevertheless, the synthetic tests suggest that a shallow break-off as imaged in the work of Paffrath, Friederich, Schmid, et al. (2021) may not be resolvable (Figure 7). The algorithm is able to fit the synthetic data in all cases within the given data uncertainty, but there is hardly any influence on the misfit by including the shallow low-velocity mantle layer (break-off). In absence of additional constraints, the rj-MCMC algorithm will prefer "simple" models with a low number of Voronoi cells (natural parsimony, e.g., Bodin et al., 2012). It therefore converges to a model with fewer cells and without break-off. In addition, the synthetic tests indicate that the surface-wave data is flexible so that different mantle structures yield similar surface-wave misfits (Figure 7). Due to the broad sensitivity kernels of surface waves, a low-velocity zone directly beneath the Moho can thus be fitted by adapting the velocities in the crust or in the slab underneath without a major influence on the residuals. For the real data model this implies that a shallow break-off cannot be reliably resolved. In the body-wave model there are some signs of break off, not in the surface-wave model, though. A better resolution could be achieved by (a) lower measurement uncertainties, (b) more accurate forward modeling (e.g., 3D sensitivity kernels), (c) additional prior information, (d) more data types (e.g., receiver

functions, gravity, Pn waves, local earthquakes for a better constrained  $v_p$  structure in the crust), (e) inclusion of anisotropy, (f) a different parameterization since a Voronoi cell model can lead to too simplified structures.

## 8. Conclusions

We combine several large data sets of Rayleigh, Love, P and S travel time measurements to obtain one 3D  $v_p$  and  $v_s$  tomographic model. At shallow depths, body wave paths from teleseismic earthquakes are mostly vertical, leading to a low resolution in the uppermost mantle and the crust. Surface waves show a decrease in resolution at larger depth, due to the period dependency of the sensitivity. Joining the different data sets allows us to image the velocity structure from the surface down to a depth of 600 km. The final model can fit both data types with similar misfit as from single-dataset inversions. However, the synthetic tests suggest that some important features such as a shallow and relatively narrow slab break-off may not be well resolvable as there are alternative models that yield a similar data fit.

The  $v_s$  structure in the final crustal model and in the crust-mantle transition zone resembles that of previous surface-wave studies. Below, the model suggests a thickened lithospheric root of the Adriatic and European plates and continuous slabs down to at least 400 km depth. A strong LVA in the shallow mantle is imaged under the Massif Central in France. There is no indication of a slab break-off in the imaged structures. The  $v_p/v_s$  structure shows no clear relation to supposed tectonic processes and may largely be influenced by trade-offs between different data types. The influence of the  $v_p/v_s$  ratio on the imaged mantle velocity geometries is, however, small.

The analysis of the model standard deviation gives additional information on the certainty of the imaged structures. It shows that the  $v_p$  structure in the crust is not well constrained and future efforts may profit from either providing additional prior information or more data, such as from local earthquakes. Also other data types may be added with the presented rj-McMC approach, for example, gravity data, as long as the forward problem can be solved efficiently. More accurate results may further be achieved by using the full 3D surface-wave sensitivity kernels. These could be updated in regular intervals, however, with a large computational effort and an increase in the memory requirement. The forward calculations during the search iterations may in turn be faster than the current approach where dispersion curves from 1D depth profiles are repeatedly calculated.

## Appendix A

Members of the AlpArray Working Group can be found at: [www.alparray.ethz.ch/en/seismic\\_network/backbone/data-policy-and-citation](http://www.alparray.ethz.ch/en/seismic_network/backbone/data-policy-and-citation) and members of the SWATH-D Working Group at: <https://doi.org/10.14470/mf7562601148>.

## Data Availability Statement

The Python scripts used for the 3D McMC tomography and the final 3D model from the joint inversion are available from E. D. Kästle (2025) and E. D. Kästle et al. (2025). The AN data is downloaded and processed with the scripts provided in Kästle and Tilmann (2023). All of the seismic data used in this study (surface- and body-wave data) is open access and freely distributed through ORFEUS and EIDA ([www.orfeus-eu.org/data/eida/](http://www.orfeus-eu.org/data/eida/)). The data comprises the following seismic networks: 1N (Malet et al., 2015), BW (University of München, 2001), C4 (CERN, 2016), CH (Swiss Seismological Service, ETH Zurich, 1983), CR (University of Zagreb, 2001), CZ (Charles University in Prague et al., 1973), FR (RESIF, 1995), G (Institut de physique du globe de Paris (IPGP) & École et Observatoire des Sciences de la Terre de Strasbourg (EOST), 1982), GE (GEOFON Data Centre, 1993), GR (Federal Institute for Geosciences & Natural Resources, 1976), GU (University of Genoa, 1967), HU (Kövesligethy Radó Seismological Observatory, 1992), HS (Hessian Agency for Nature Conservation & Geology, 2012), IU (Albuquerque Seismological Laboratory/USGS, 2014), IV (Istituto Nazionale di Geofisica e Vulcanologia (INGV), 2005), MN (MedNet Project Partner Institutions, 1990), MT (OMIV Project Partner Institutions, 2006), NI (OGS (Istituto Nazionale di Oceanografia e di Geofisica Sperimentale) & University of Trieste, 2002), OE (ZAMG - Zentralanstalt für Meteorologie und Geodynamik, 1987), OX (Istituto Nazionale di Oceanografia e di Geofisica Sperimentale - OGS, 2016), RD (RESIF, 2018), RF (University of Trieste, 1993), SI (ZAMG - Central Institute for Meteorology and Geodynamics, Austria, 2006), SK (ESI SAS; Former GPI SAS (Geophysical Institute Of The Slovak Academy Of Sciences), 2004), SL (Slovenian Environment Agency, 1990), ST (Geological Survey-Provincia Autonoma di Trento, 1981), SX (University of Leipzig, 2001), TH (Friedrich-

Schiller-Universitaet Jena, 2009) YW (RESIF - Réseau Sismologique et géodésique Français, 2017), Z3 (AlpArray Seismic Network, 2015), ZH (Deschamps & Beucler, 2013), ZS (Heit et al., 2017).

## Acknowledgments

We express our thanks to the editor Fenglin Niu, to the reviewer Andrew Curtis and to one anonymous reviewer for their insightful comments. The authors are grateful to the AlpArray Seismic Network Team ([www.alparray.ethz.ch/seismic\\_network/backbone/management/](http://www.alparray.ethz.ch/seismic_network/backbone/management/)). We also want to thank all the colleagues associated with the AlpArray and the 4DMB programs that helped to make this work possible. Data processing was done with the Python software *ants\_2* provided by L. Ermert ([github.com/lermert/ants\\_2](https://github.com/lermert/ants_2)) and Obspy (Beyreuther et al., 2010). We want to thank the HPC services of the Zedat, Freie Universität Berlin for the computational resources (Bennett et al., 2020). Ray tracing is based on the scikit-fmm software ([github.com/scikit-fmm/scikit-fmm](https://github.com/scikit-fmm/scikit-fmm)). Several colormaps from Crameri (2018) are used in this work. EK has received funding from the German Science Foundation (SPP-2017, Project Ha 2403/21-1), as well as MP (SPP-2017, Project FR 1146/12-1). Open Access funding enabled and organized by Projekt DEAL.

## References

- Aki, K. (1957). Space and time spectra of stationary stochastic waves, with special reference to microtremors. *Bulletin of the Earthquake Research Institute*, 35, 415–456.
- Albuquerque Seismological Laboratory/USGS. (2014). Global Seismograph Network (GSN - IRIS/USGS) [Dataset]. *International Federation of Digital Seismograph Networks*. <https://doi.org/10.7914/SN/IU>
- AlpArray Seismic Network. (2015). AlpArray Seismic Network (AASN) temporary component [Dataset]. *AlpArray Working Group*. [https://doi.org/10.12686/ALPARRAY/Z3\\_2015](https://doi.org/10.12686/ALPARRAY/Z3_2015)
- Antolik, M., Gu, Y. J., Ekström, G., & Dziewonski, A. M. (2003). J362D28: A new joint model of compressional and shear velocity in the Earth's mantle. *Geophysical Journal International*, 153(2), 443–466. <https://doi.org/10.1046/j.1365-246x.2003.01910.x>
- Bennett, L., Melchers, B., & Proppe, B. (2020). *Curta: A General-purpose High-Performance Computer at ZEDAT*. Freie Universität Berlin. <https://doi.org/10.17169/refubium-26754>
- Bensen, G., Ritzwoller, M., Barmin, M., Levshin, A. L., Lin, F., Moschetti, M., et al. (2007). Processing seismic ambient noise data to obtain reliable broad-band surface wave dispersion measurements. *Geophysical Journal International*, 169(3), 1239–1260. <https://doi.org/10.1111/j.1365-246x.2007.03374.x>
- Berteussen, K.-A. (1977). Moho depth determinations based on spectral-ratio analysis of NORSAR long-period P waves. *Physics of the Earth and Planetary Interiors*, 15(1), 13–27. [https://doi.org/10.1016/0031-9201\(77\)90006-1](https://doi.org/10.1016/0031-9201(77)90006-1)
- Beyreuther, M., Barsch, R., Krischer, L., Megies, T., Behr, Y., & Wassermann, J. (2010). ObsPy: A Python toolbox for seismology. *Seismological Research Letters*, 81(3), 530–533. <https://doi.org/10.1785/gssrl.81.3.530>
- Bodin, T. (2010). *Transdimensional approaches to geophysical inverse problems*. The Australian National University. <https://doi.org/10.25911/5D5FCEC8BD08E4>
- Bodin, T., & Sambridge, M. (2009). Seismic tomography with the reversible jump algorithm. *Geophysical Journal International*, 178(3), 1411–1436. <https://doi.org/10.1111/j.1365-246x.2009.04226.x>
- Bodin, T., Sambridge, M., Rawlinson, N., & Arroucau, P. (2012). Transdimensional tomography with unknown data noise. *Geophysical Journal International*, 189(3), 1536–1556. <https://doi.org/10.1111/j.1365-246x.2012.05414.x>
- CERN. (2016). CERN Seismic Network [Dataset]. *International Federation of Digital Seismograph Networks*. <https://doi.org/10.12686/sed/networks/c4>
- Charles University in Prague, Institute of Geonics, Institute of Geophysics, Academy of Sciences of the Czech Republic, Institute of Physics of the Earth Masaryk University (Czech), & Institute of Rock Structure and Mechanics. (1973). Czech Regional Seismic Network [Dataset]. *International Federation of Digital Seismograph Networks*. <https://doi.org/10.7914/SN/CZ>
- Crameri, F. (2018). Scientific color maps. <https://doi.org/10.5281/zenodo.1243862>
- Deschamps, A., & Beucler, E. (2013). RESIF - POSA [Dataset]. *RESIF - Réseau Sismologique et géodésique Français*. <https://doi.org/10.15778/resif.zh2016>
- Dewey, J., Helman, M., Knott, S., Turco, E., & Hutton, D. (1989). Kinematics of the western Mediterranean. *Geological Society, London, Special Publications*, 45(1), 265–283. <https://doi.org/10.1144/gsl.sp.1989.045.01.15>
- Ekström, G., Abers, G. A., & Webb, S. C. (2009). Determination of surface-wave phase velocities across USArray from noise and Aki's spectral formulation. *Geophysical Research Letters*, 36(18), L18301. <https://doi.org/10.1029/2009gl039131>
- El-Sharkawy, A., Meier, T., Lebedev, S., Behrmann, J. H., Hamada, M., Cristiano, L., et al. (2020). The slab puzzle of the Alpine-Mediterranean region: Insights from a new, high-resolution, shear wave velocity model of the upper mantle. *Geochemistry, Geophysics, Geosystems*, 21(8), e2020GC008993. <https://doi.org/10.1029/2020gc008993>
- ESI SAS; Former GPI SAS (Geophysical Institute Of The Slovak Academy Of Sciences). (2004). National Network of Seismic Stations of Slovakia [Dataset]. *GFZ Data Services*. <https://doi.org/10.14470/FX099882>
- Fang, H., Yao, H., Zhang, H., Huang, Y.-C., & van der Hilst, R. D. (2015). Direct inversion of surface wave dispersion for three-dimensional shallow crustal structure based on ray tracing: Methodology and application. *Geophysical Journal International*, 201(3), 1251–1263. <https://doi.org/10.1093/gji/ggv080>
- Federal Institute for Geosciences, & Natural Resources. (1976). German Regional Seismic Network (GRSN) [Dataset]. *Bundesanstalt für Geowissenschaften und Rohstoffe*. <https://doi.org/10.25928/MBX6-HR74>
- Fichtner, A., van Herwaarden, D.-P., Afanasiev, M., Simuté, S., Krischer, L., Çubuk-Sabancı, Y., et al. (2018). The collaborative seismic Earth model: Generation 1. *Geophysical Research Letters*, 45(9), 4007–4016. <https://doi.org/10.1029/2018gl077338>
- Fichtner, A., & Villaseñor, A. (2015). Crust and upper mantle of the western Mediterranean—Constraints from full-waveform inversion. *Earth and Planetary Science Letters*, 428, 52–62. <https://doi.org/10.1016/j.epsl.2015.07.038>
- Fichtner, A., Zunino, A., & Gebraad, L. (2019). Hamiltonian Monte Carlo solution of tomographic inverse problems. *Geophysical Journal International*, 216(2), 1344–1363. <https://doi.org/10.1093/gji/ggy496>
- Fox, M., Herman, F., Kissling, E., & Willett, S. D. (2015). Rapid exhumation in the Western Alps driven by slab detachment and glacial erosion. *Geology*, 43(5), 379–382. <https://doi.org/10.1130/g36411.1>
- Fox, M., Herman, F., Willett, S. D., & Schmid, S. M. (2016). The exhumation history of the European Alps inferred from linear inversion of thermochronometric data. *American Journal of Science*, 316(6), 505–541. <https://doi.org/10.2475/06.2016.01>
- Friedrich-Schiller-Universitaet Jena, I. F. G. (2009). Thüringer Seismologisches Netz [Dataset]. *International Federation of Digital Seismograph Networks*. <https://doi.org/10.7914/SN/TH>
- Galetti, E., Curtis, A., Meles, G. A., & Baptie, B. (2015). Uncertainty loops in travel-time tomography from nonlinear wave physics. *Physical Review Letters*, 114(14), 148501. <https://doi.org/10.1103/physrevlett.114.148501>
- Gelman, A., Carlin, J. B., Stern, H. S., & Rubin, D. B. (1995). *Bayesian data analysis*. Chapman and Hall/CRC.
- GEOFON Data Centre. (1993). GEOFON Seismic Network [Dataset]. *Deutsches GeoForschungsZentrum GFZ*. <https://doi.org/10.14470/TR560404>
- Geological Survey-Provincia Autonoma di Trento. (1981). Trentino Seismic Network [Dataset]. *International Federation of Digital Seismograph Networks*. <https://doi.org/10.7914/SN/ST>
- Giacomuzzi, G., Civalleri, M., De Gori, P., & Chiarabba, C. (2012). A 3D Vs model of the upper mantle beneath Italy: Insight on the geodynamics of central Mediterranean. *Earth and Planetary Science Letters*, 335, 105–120. <https://doi.org/10.1016/j.epsl.2012.05.004>



- Golos, E., Fang, H., Yao, H., Zhang, H., Burdick, S., Vernon, F., et al. (2018). Shear wave tomography beneath the United States using a joint inversion of surface and body waves. *Journal of Geophysical Research: Solid Earth*, 123(6), 5169–5189. <https://doi.org/10.1029/2017jb014894>
- Green, P. J., & Hastie, D. I. (2009). Reversible jump MCMC. *Genetics*, 155(3), 1391–1403.
- Handy, M. R., Schmid, S. M., Bousquet, R., Kissling, E., & Bernoulli, D. (2010). Reconciling plate-tectonic reconstructions of Alpine Tethys with the geological–geophysical record of spreading and subduction in the Alps. *Earth-Science Reviews*, 102(3–4), 121–158. <https://doi.org/10.1016/j.earscirev.2010.06.002>
- Handy, M. R., Schmid, S. M., Paffrath, M., Friederich, W., & the AlpArray Working Group. (2021). Orogenic lithosphere and slabs in the greater Alpine area—interpretations based on teleseismic P-wave tomography. *Solid Earth*, 12(11), 2633–2669. <https://doi.org/10.5194/se-12-2633-2021>
- Handy, M. R., Ustaszewski, K., & Kissling, E. (2015). Reconstructing the Alps–Carpathians–Dinarides as a key to understanding switches in subduction polarity, slab gaps and surface motion. *International Journal of Earth Sciences*, 104, 1–26. <https://doi.org/10.1007/s00531-014-1060-3>
- Hawkins, R., Bodin, T., Sambridge, M., Choblet, G., & Husson, L. (2019). Trans-dimensional surface reconstruction with different classes of parameterization. *Geochemistry, Geophysics, Geosystems*, 20(1), 505–529. <https://doi.org/10.1029/2018gc008022>
- Hawkins, R., & Sambridge, M. (2015). Geophysical imaging using trans-dimensional trees. *Geophysical Journal International*, 203(2), 972–1000. <https://doi.org/10.1093/gji/ggv326>
- Heit, B., Cristiano, L., Haberland, C., Tilmann, F., Pesaresi, D., Jia, Y., et al. (2021). The SWATH-D seismological network in the Eastern Alps. *Seismological Society of America*, 92(3), 1592–1609. <https://doi.org/10.1785/0220200377>
- Heit, B., Weber, M., Tilmann, F., Haberland, C., Jia, Y., Carraro, C., et al. (2017). The Swath-D Seismic Network in Italy and Austria [Dataset]. *GFZ Data Services*. <https://doi.org/10.14470/MF7562601148>
- Hessian Agency for Nature Conservation, Environment, & Geology. (2012). Hessischer Erdbebendienst [Dataset]. *International Federation of Digital Seismograph Networks*. <https://doi.org/10.7914/SN/HS>
- Hetényi, G., Molinari, I., Clinton, J., Bokelmann, G., Bondár, I., Crawford, W. C., et al. (2018). The AlpArray seismic network: A large-scale European experiment to image the Alpine orogen. *Surveys in Geophysics*, 39(5), 1009–1033. <https://doi.org/10.1007/s10712-018-9472-4>
- Institut de physique du globe de Paris (IPGP), & École et Observatoire des Sciences de la Terre de Strasbourg (EOST). (1982). GEOSCOPE, French Global Network of broad band seismic stations [Dataset]. *Institut de physique du globe de Paris (IPGP), Université de Paris*. <https://doi.org/10.18715/GEOSCOPE.G>
- Istituto Nazionale di Geofisica e Vulcanologia (INGV). (2005). Rete Sismica Nazionale (RSN) [Dataset]. *Istituto Nazionale di Geofisica e Vulcanologia (INGV)*. <https://doi.org/10.13127/SD/X0FXNH7QFY>
- Istituto Nazionale di Oceanografia e di Geofisica Sperimentale - OGS. (2016). North-East Italy Seismic Network [Dataset]. *International Federation of Digital Seismograph Networks*. <https://doi.org/10.7914/SN/OX>
- Jozi Najafabadi, A., Haberland, C., Le Breton, E., Handy, M. R., Verwater, V. F., Heit, B., & Weber, M. (2022). Constraints on crustal structure in the vicinity of the Adriatic Indenter (European Alps) from Vp and Vp/Vs local earthquake tomography. *Journal of Geophysical Research: Solid Earth*, 127(2), e2021JB023160. <https://doi.org/10.1029/2021jb023160>
- Kästle, E., El-Sharkawy, A., Boschi, L., Meier, T., Rosenberg, C., Bellahsen, N., et al. (2018). Surface wave tomography of the Alps using ambient-noise and earthquake phase velocity measurements. *Journal of Geophysical Research: Solid Earth*, 123(2), 1770–1792. <https://doi.org/10.1002/2017jb014698>
- Kästle, E., Molinari, I., Boschi, L., Kissling, E., & the AlpArray Working Group. (2022). Azimuthal anisotropy from eikonal tomography: Example from ambient-noise measurements in the AlpArray network. *Geophysical Journal International*, 229(1), 151–170. <https://doi.org/10.1093/gji/ggab453>
- Kästle, E., Rosenberg, C., Boschi, L., Bellahsen, N., Meier, T., & El-Sharkawy, A. (2020). Slab break-offs in the Alpine subduction zone. *International Journal of Earth Sciences*, 109(2), 587–603. <https://doi.org/10.1007/s00531-020-01821-z>
- Kästle, E., Tilmann, F., & the AlpArray and Swath-D Working Groups. (2024). Anisotropic reversible-jump MCMC shear-velocity tomography of the eastern Alpine crust. *Geochemistry, Geophysics, Geosystems*, 25(3), e2023GC011238. <https://doi.org/10.1029/2023gc011238>
- Kästle, E. D. (2025). baytomo3d - 3D Transdimensional Reversible Jump MCMC Tomography [Dataset]. *GFZ Data Services*. <https://doi.org/10.5880/fidgeo.2025.011>
- Kästle, E. D., Paffrath, M., & El-Sharkawy, A. (2025). Subsurface Vp and Vs model of crust and upper mantle under the Alps [Dataset]. *GFZ Data Services*. <https://doi.org/10.5880/fidgeo.2025.009>
- Kästle, E. D., Soomro, R., Weemstra, C., Boschi, L., & Meier, T. (2016). Two-receiver measurements of phase velocity: Cross-validation of ambient-noise and earthquake-based observations. *Geophysical Journal International*, 207(3), 1493–1512. <https://doi.org/10.1093/gji/ggw341>
- Kästle, E. D., & Tilmann, F. (2023). Data Download and Processing [Dataset]. *Zenodo*. <https://doi.org/10.5281/zenodo.10428135>
- Kennett, B., & Engdahl, E. (1991). Traveltimes for global earthquake location and phase identification. *Geophysical Journal International*, 105(2), 429–465. <https://doi.org/10.1111/j.1365-246x.1991.tb06724.x>
- Koulakov, I., Kaban, M., Tesauro, M., & Cloetingh, S. (2009). P- and S-velocity anomalies in the upper mantle beneath Europe from tomographic inversion of ISC data. *Geophysical Journal International*, 179(1), 345–366. <https://doi.org/10.1111/j.1365-246x.2009.04279.x>
- Kövesligethy Radó Seismological Observatory, H. A. O. S. M. C. G. K. (1992). Hungarian National Seismological Network [Dataset]. *GFZ Data Services*. <https://doi.org/10.14470/UH028726>
- Kuhlemann, J. (2007). Paleogeographic and paleotopographic evolution of the Swiss and Eastern Alps since the Oligocene. *Global and Planetary Change*, 58(1–4), 224–236. <https://doi.org/10.1016/j.gloplacha.2007.03.007>
- Küperkoch, L., Meier, T., Lee, J., Friederich, W., & the EGELADOS Working Group. (2010). Automated determination of P-phase arrival times at regional and local distances using higher order statistics. *Geophysical Journal International*, 181, 1159–1170. <https://doi.org/10.1111/j.1365-246X.2010.04570.x>
- Lippitsch, R., Kissling, E., & Ansgor, J. (2003). Upper mantle structure beneath the Alpine orogen from high-resolution teleseismic tomography. *Journal of Geophysical Research*, 108(B8), 2376. <https://doi.org/10.1029/2002jb002016>
- Lu, Y., Stehly, L., Paul, A., & the AlpArray Working Group. (2018). High-resolution surface wave tomography of the European crust and uppermost mantle from ambient seismic noise. *Geophysical Journal International*, 214(2), 1136–1150. <https://doi.org/10.1093/gji/ggy188>
- Lüschen, E., Lammerer, B., Gebrande, H., Millahn, K., Nicolich, R., Group, T. W., et al. (2004). Orogenic structure of the Eastern Alps, Europe, from TRANSALP deep seismic reflection profiling. *Tectonophysics*, 388(1–4), 85–102. <https://doi.org/10.1016/j.tecto.2004.07.024>
- Malet, J.-P., Hibert, C., Radiguet, M., Gautier, S., Larose, E., Amitrano, D., et al. (2015). RESIF - SISMOB [Dataset]. *RESIF - Réseau Sismologique et géodésique Français*. <https://doi.org/10.15778/resif.1n2015>

- MedNet Project Partner Institutions. (1990). Mediterranean Very Broadband Seismographic Network (MedNet) [Dataset]. *Istituto Nazionale di Geofisica e Vulcanologia (INGV)*. <https://doi.org/10.13127/SD/FBBBTD6Q>
- Meier, T., Dietrich, K., Stöckert, B., & Harjes, H.-P. (2004). One-dimensional models of shear wave velocity for the eastern Mediterranean obtained from the inversion of Rayleigh wave phase velocities and tectonic implications. *Geophysical Journal International*, 156(1), 45–58. <https://doi.org/10.1111/j.1365-246x.2004.02121.x>
- Metropolis, N., Rosenbluth, A. W., Rosenbluth, M. N., Teller, A. H., & Teller, E. (1953). Equation of state calculations by fast computing machines. *Journal of Chemical Physics*, 21(6), 1087–1092. <https://doi.org/10.1063/1.1699114>
- Mitterbauer, U., Behm, M., Brückl, E., Lippitsch, R., Guterch, A., Keller, G. R., et al. (2011). Shape and origin of the East-Alpine slab constrained by the ALPASS teleseismic model. *Tectonophysics*, 510(1), 195–206. <https://doi.org/10.1016/j.tecto.2011.07.001>
- Mroczek, S., Tilmann, F., Pleuger, J., Yuan, X., Heit, B., & the Swath-D and AlpArray Working Groups. (2023). Investigating the Eastern Alpine–Dinaric transition with teleseismic receiver functions: Evidence for subducted European crust. *Earth and Planetary Science Letters*, 609, 118096. <https://doi.org/10.1016/j.epsl.2023.118096>
- Müller, G. (1971). Approximate treatment of elastic body waves in media with spherical symmetry. *Geophysical Journal International*, 23(4), 435–449. <https://doi.org/10.1111/j.1365-246x.1971.tb01835.x>
- Nouibat, A., Stehly, L., Paul, A., Schwartz, S., Bodin, T., Dumont, T., et al. (2022). Lithospheric transdimensional ambient-noise tomography of W-Europe: Implications for crustal-scale geometry of the W-Alps. *Geophysical Journal International*, 229(2), 862–879. <https://doi.org/10.1093/gji/ggab520>
- Nunn, C., Roecker, S. W., Priestley, K. F., Liang, X., & Gilligan, A. (2014). Joint inversion of surface waves and teleseismic body waves across the Tibetan collision zone: The fate of subducted Indian lithosphere. *Geophysical Journal International*, 198(3), 1526–1542. <https://doi.org/10.1093/gji/ggu193>
- OGS (Istituto Nazionale di Oceanografia e di Geofisica Sperimentale), & University of Trieste. (2002). North-East Italy Broadband Network [Dataset]. *International Federation of Digital Seismograph Networks*. <https://doi.org/10.7914/SN/NI>
- OMIV Project Partner Institutions. (2006). OMIV French Landslide Observatory [Dataset]. *RESIF - Réseau Sismologique et géodésique Français*. <https://doi.org/10.15778/RESIF.MT>
- Paffrath, M., Friederich, W., & the AlpArray and SWATH-D Working Groups. (2021). Teleseismic P-waves at the AlpArray seismic network: Wave fronts, absolute traveltimes and traveltime residuals. *Solid Earth*, 12(7), 1635–1660. <https://doi.org/10.5194/se-12-1635-2021>
- Paffrath, M., Friederich, W., Schmid, S. M., Handy, M. R., & the AlpArray and Swath-D Working Groups. (2021). Imaging structure and geometry of slabs in the greater Alpine area—A P-wave travel-time tomography using AlpArray Seismic Network data. *Solid Earth*, 12(11), 2671–2702. <https://doi.org/10.5194/se-12-2671-2021>
- Paul, A., Pedersen, H. A., Bodin, T., Kästle, E., Soergel, D., Alder, C., et al. (2024). New Developments in Passive Seismic Imaging and Monitoring Methodological advances on seismic noise imaging in the Alpine area. *Comptes Rendus Geoscience*, 356(S4), 5–39. <https://doi.org/10.5802/crgeos.261>
- Plomerová, J., Žlebčíková, H., Hetényi, G., Vecsey, L., & Babuška, V. (2022). Two subduction-related heterogeneities beneath the Eastern Alps and the Bohemian Massif imaged by high-resolution P-wave tomography. *Solid Earth*, 13(1), 251–270. <https://doi.org/10.5194/se-13-251-2022>
- Rappisi, F., VanderBeek, B., Faccenda, M., Morelli, A., & Molinari, I. (2022). Slab geometry and upper mantle flow patterns in the Central Mediterranean from 3D anisotropic P-wave tomography. *Journal of Geophysical Research: Solid Earth*, 127(5), e2021JB023488. <https://doi.org/10.1029/2021jb023488>
- RESIF. (1995). RESIF-RLBP French Broad-band network, RESIF-RAP strong motion network and other seismic stations in metropolitan France [Dataset]. *RESIF - Réseau Sismologique et géodésique Français*. <https://doi.org/10.15778/RESIF.FR>
- RESIF. (2018). CEA/DASE broad-band permanent network in metropolitan France [Dataset]. *RESIF - Réseau Sismologique et géodésique Français*. <https://doi.org/10.15778/RESIF.RD>
- RESIF - Réseau Sismologique et géodésique Français. (2017). Earthquake swarm Maurienne 2017- (French Alps) [Dataset]. *International Federation of Digital Seismograph Networks*. <https://doi.org/10.15778/RESIF.YW2017>
- Sambridge, M. (2014). A parallel tempering algorithm for probabilistic sampling and multimodal optimization. *Geophysical Journal International*, 196(1), 357–374. <https://doi.org/10.1093/gji/ggt342>
- Schlunegger, F., & Castellort, S. (2016). Immediate and delayed signal of slab breakoff in Oligo/Miocene Molasse deposits from the European Alps. *Scientific Reports*, 6(1), 31010. <https://doi.org/10.1038/srep31010>
- Schlunegger, F., & Kissling, E. (2022). Slab load controls beneath the Alps on the source-to-sink sedimentary pathways in the Molasse basin. *Geosciences*, 12(6), 226. <https://doi.org/10.3390/geosciences12060226>
- Schmid, S., & Kissling, E. (2000). The arc of the western Alps in the light of geophysical data on deep crustal structure. *Tectonics*, 19(1), 62–85. <https://doi.org/10.1029/1999tc900057>
- Schmid, S. M., Bernoulli, D., Fügenschuh, B., Matenco, L., Schefer, S., Schuster, R., et al. (2008). The Alpine-Carpathian-Dinaric orogenic system: Correlation and evolution of tectonic units. *Swiss Journal of Geosciences*, 101(1), 139–183. <https://doi.org/10.1007/s00015-008-1247-3>
- Schmid, S. M., Fügenschuh, B., Kissling, E., & Schuster, R. (2004). Tectonic map and overall architecture of the Alpine orogen. *Eclogae Geologicae Helveticae*, 97(1), 93–117. <https://doi.org/10.1007/s00015-004-1113-x>
- Schmid, S. M., Scharf, A., Handy, M. R., & Rosenberg, C. L. (2013). The Tauern Window (Eastern Alps, Austria): A new tectonic map, with cross-sections and a tectonometamorphic synthesis. *Swiss Journal of Geosciences*, 106(1), 1–32. <https://doi.org/10.1007/s00015-013-0123-y>
- Sen, M. K., & Stoffa, P. L. (2013). *Global optimization methods in geophysical inversion*. Cambridge University Press. <https://doi.org/10.1017/CBO9780511997570>
- Simmons, N., Myers, S., Morency, C., Chiang, A., & Knapp, D. (2021). SPiRaL: A multiresolution global tomography model of seismic wave speeds and radial anisotropy variations in the crust and mantle. *Geophysical Journal International*, 227(2), 1366–1391. <https://doi.org/10.1093/gji/ggab277>
- Slovenian Environment Agency. (1990). Seismic Network of the Republic of Slovenia [Dataset]. *International Federation of Digital Seismograph Networks*. <https://doi.org/10.7914/SN/SL>
- Soomro, R., Weidle, C., Cristiano, L., Lebedev, S., Meier, T., & Group, P. W. (2016). Phase velocities of Rayleigh and Love waves in central and northern Europe from automated, broad-band, interstation measurements. *Geophysical Journal International*, 204(1), 517–534. <https://doi.org/10.1093/gji/ggv462>
- Stampfli, G. M., & Borel, G. (2002). A plate tectonic model for the Paleozoic and Mesozoic constrained by dynamic plate boundaries and restored synthetic oceanic isochrons. *Earth and Planetary Science Letters*, 196(1–2), 17–33. [https://doi.org/10.1016/S0012-821X\(01\)00588-x](https://doi.org/10.1016/S0012-821X(01)00588-x)
- Swiss Seismological Service, ETH Zurich. (1983). National Seismic Networks of Switzerland [Dataset]. *ETH Zürich*. <https://doi.org/10.12686/SED/NETWORKS/CH>

- Thrustarson, S., van Herwaarden, D.-P., Noe, S., Josef Schiller, C., & Fichtner, A. (2024). REVEAL: A global full-waveform inversion model. *Bulletin of the Seismological Society of America*, 114(3), 1392–1406. <https://doi.org/10.1785/0120230273>
- Tilmann, F., Sadeghisorkhani, H., & Mauerberger, A. (2020). Another look at the treatment of data uncertainty in Markov chain Monte Carlo inversion and other probabilistic methods. *Geophysical Journal International*, 222(1), 388–405. <https://doi.org/10.1093/gji/ggaa168>
- University of Genoa. (1967). Regional Seismic Network of North Western Italy [Dataset]. *International Federation of Digital Seismograph Networks*. <https://doi.org/10.7914/SN/GU>
- University of Leipzig. (2001). SXNET Saxon Seismic Network [Dataset]. *International Federation of Digital Seismograph Networks*. <https://doi.org/10.7914/SN/SX>
- University of München, G. O., Department of Earth and Environmental Sciences. (2001). BayernNetz [Dataset]. *International Federation of Digital Seismograph Networks*. <https://doi.org/10.7914/SN/BW>
- University of Trieste. (1993). Friuli Venezia Giulia Accelerometric Network [Dataset]. *International Federation of Digital Seismograph Networks*. <https://doi.org/10.7914/SN/RF>
- University of Zagreb. (2001). Croatian Seismograph Network [Dataset]. *International Federation of Digital Seismograph Networks*. <https://doi.org/10.7914/SN/CR>
- Ustaszewski, K., Schmid, S. M., Fügenschuh, B., Tischler, M., Kissling, E., & Spakman, W. (2008). A map-view restoration of the Alpine-Carpathian-Dinaridic system for the Early Miocene. *Swiss Journal of Geosciences*, 101(S1), 273–294. <https://doi.org/10.1007/s00015-008-1288-7>
- von Blanckenburg, F., & Davies, J. H. (1995). Slab breakoff: A model for syncollisional magmatism and tectonics in the Alps. *Tectonics*, 14(1), 120–131. <https://doi.org/10.1029/94tc02051>
- Wathelet, M., Chatelain, J.-L., Cornou, C., Giulio, G. D., Guillier, B., Ohrnberger, M., & Savvaidis, A. (2020). Geopsy: A user-friendly open-source tool set for ambient vibration processing. *Seismological Research Letters*, 91(3), 1878–1889. <https://doi.org/10.1785/0220190360>
- West, M., Gao, W., & Grand, S. (2004). A simple approach to the joint inversion of seismic body and surface waves applied to the southwest US. *Geophysical Research Letters*, 31(15), L15615. <https://doi.org/10.1029/2004gl020373>
- ZAMG - Central Institute for Meteorology and Geodynamics, Austria. (2006). Sudtirol Network, Austria [Dataset]. *International Federation of Digital Seismograph Networks*. Retrieved from <https://www.fdsn.org/networks/detail/SI/>
- ZAMG - Zentralanstalt für Meteorologie und Geodynamik. (1987). Austrian Seismic Network [Dataset]. *International Federation of Digital Seismograph Networks*. <https://doi.org/10.7914/SN/OE>
- Zhang, X., & Curtis, A. (2020). Seismic tomography using variational inference methods. *Journal of Geophysical Research: Solid Earth*, 125(4), e2019JB018589. <https://doi.org/10.1029/2019jb018589>
- Zhang, X., & Curtis, A. (2021). Bayesian geophysical inversion using invertible neural networks. *Journal of Geophysical Research: Solid Earth*, 126(7), e2021JB022320. <https://doi.org/10.1029/2021jb022320>
- Zhang, X., Curtis, A., Galetti, E., & De Ridder, S. (2018). 3-D Monte Carlo surface wave tomography. *Geophysical Journal International*, 215(3), 1644–1658. <https://doi.org/10.1093/gji/ggy362>
- Zhang, X., Roy, C., Curtis, A., Nowacki, A., & Baptie, B. (2020). Imaging the subsurface using induced seismicity and ambient noise: 3-D tomographic Monte Carlo joint inversion of earthquake body wave traveltimes and surface wave dispersion. *Geophysical Journal International*, 222(3), 1639–1655. <https://doi.org/10.1093/gji/ggaa230>
- Zhao, L., Paul, A., Malusà, M. G., Xu, X., Zheng, T., Solarino, S., et al. (2016). Continuity of the Alpine slab unraveled by high-resolution P wave tomography. *Journal of Geophysical Research: Solid Earth*, 121(12), 8720–8737. <https://doi.org/10.1002/2016jb013310>
- Zhao, L., Paul, A., Solarino, S., & RESIF. (2016). Seismic network YP: CIFALPS temporary experiment (China-Italy-France Alps seismic transect). *RESIF (Réseau Sismologique et Géodésique Français)*. <https://doi.org/10.15778/resif.yp2012>
- Zhu, H., Bozdağ, E., & Tromp, J. (2015). Seismic structure of the European upper mantle based on adjoint tomography. *Geophysical Journal International*, 201(1), 18–52. <https://doi.org/10.1093/gji/ggu492>